HHS Public Access

Author manuscript

Cell Rep. Author manuscript; available in PMC 2022 September 03.

Published in final edited form as:

Cell Rep. 2022 August 23; 40(8): 111254. doi:10.1016/j.celrep.2022.111254.

Heterotropic roles of divalent cations in the establishment of allostery and affinity maturation of integrin αXβ2

Pragya Manandhar[1,3], **Zahra Mazhar**[1,3], **Omar Abousaway**[1,3], **Collins Aboagye**[1,3], **Zeinab Moussa**[1,3], **Daniel Lim**[1], **Tannon Yu**[1,4], **James Byrnes**[2], **James M. Briggs**[1], **Mehmet Sen**[1,5,*]

[1]Department of Biology and Biochemistry, University of Houston, Houston, TX 77204, USA

[2]National Synchrotron Light Source II, Brookhaven National Laboratory, Upton, NY 11973, USA

[3]These authors contributed equally

[4]Present address: Information Innovation & Insight, Texas Workforce Commission, Austin, TX 78701, USA

[5]Lead contact

SUMMARY

Allosteric activation and silencing of leukocyte β2-integrins transpire through cation-dependent structural changes, which mediate integrin biosynthesis and recycling, and are essential to designing leukocyte-specific drugs. Stepwise addition of Mg^{2+} reveals two mutually coupled events for the αXβ2 ligand-binding domain—the αX I-domain—corresponding to allostery establishment and affinity maturation. Electrostatic alterations in the Mg^{2+}-binding site establish long-range couplings, leading to both pH− and Mg^{2+}-occupancy-dependent biphasic stability change in the αX I-domain fold. The ligand-binding sensorgrams show composite affinity events for the αX I-domain accounting for the multiplicity of the αX I-domain conformational states existing in the solution. On cell surfaces, increasing Mg^{2+} concentration enhanced adhesiveness of αXβ2. This work highlights how intrinsically flexible pH− and cation-sensitive architecture endows a unique dynamic continuum to the αI-domain structure on the intact integrin, thereby revealing the importance of allostery establishment and affinity maturation in both extracellular and intracellular integrin events.

*Correspondence: msen2@cougarnet.uh.edu.

AUTHOR CONTRIBUTIONS

M.S. and J.M.B. conceived the work and wrote the manuscript; P.M. prepared the αX I-domain, carried out and processed ITC, DSF, SPR, and SAXS experimental data, and wrote the manuscript; Z. Mazhar ran neMD/MC and NMA simulations and wrote the manuscript; C.A. prepared the NMR samples and collected the data; O.A. assigned the backbone chemical shifts and wrote the manuscript; J.B. collected and analyzed SAXS data; T.Y. helped with protein expression, purification, and manuscript proofreading; D.L. extrapolated the 3D-SAXS figure; Z. Moussa performed the cell-based assays; and all of the authors reviewed the manuscript and approved its final version.

SUPPLEMENTAL INFORMATION

Supplemental information can be found online at https://doi.org/10.1016/j.celrep.2022.111254.

DECLARATION OF INTERESTS

The authors declare no competing interests.

INCLUSION AND DIVERSITY

One or more of the authors of this paper self-identifies as an underrepresented minority in science.

Graphical abstract

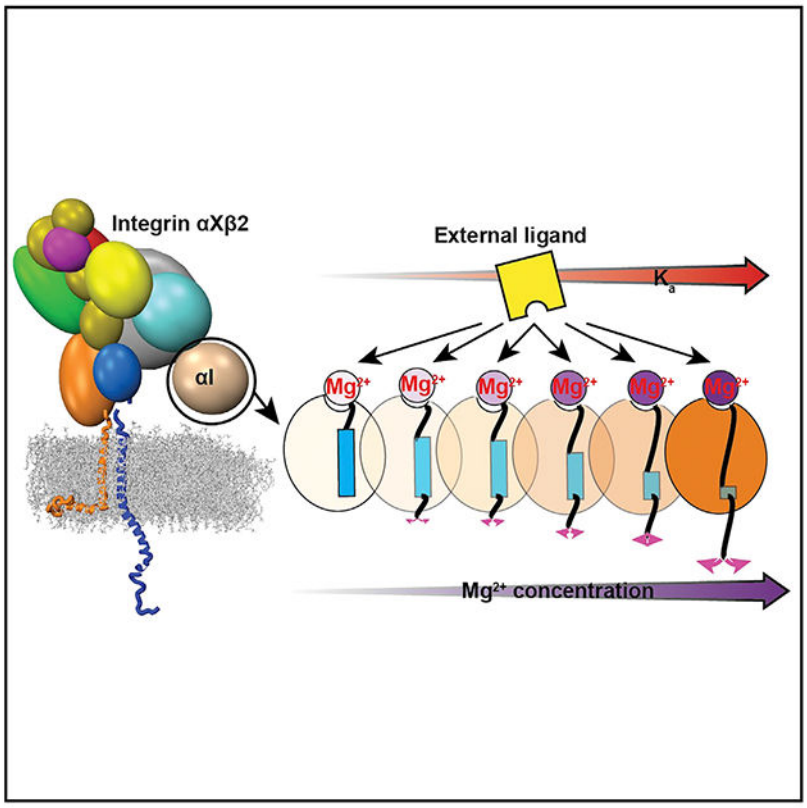

In brief

Manandhar et al. show that αXβ2 binds to dications, particularly Mg^{2+} and Ca^{2+}, which modulate its affinity by altering the shape of the αXβ2 ligand-binding domain and the ionization of the acidic residues in the cation-binding site. These findings elaborate the roles of integrin-dication interactions in integrin biosynthesis and recycling.

INTRODUCTION

Integrins are a large family of α/β heterodimeric metalloreceptors that are unique to metazoans. Nine of 18 α subunits that bind to the external ligands through the β subunits are called αI-less integrins. The remaining 9 α subunits that have acquired an “Inserted” domain (αI-domain), accordingly called αI-integrins (Figures 1, S1A, and S1B), form specialized integrins unique to vertebrates, and thus, the αI-integrins are a recent divergence. Both αI and αI-less integrins relay bidirectional, divalent cation-dependent signals (outside-in and inside-out) through highly concerted inter- and intra-domain conformational changes (Figures 1A–1E). (Hynes, 2002; Springer and Dustin, 2012) Collectively, these structural changes equilibrate uniquely for each integrin in response to the tensile force created by the actin cytoskeleton and are the main regulatory drivers of integrin affinity to their extracellular and intracellular ligands (Nordenfelt et al., 2017).

The αI-domain protrudes from the α subunits and allosterically regulates its affinity between the closed/low-affinity and the open/high-affinity states. The metal ion-dependent adhesion site (MIDAS) houses a Mg^{2+} ion, which coordinates acidic side chains from the "external ligand," and is relatively buried and surrounded by invariant hydrophobic residues (Figures 1A–1C and S1C–S1E) (Sen and Legge, 2007; Sen et al., 2013). All of the MIDAS residues and the surrounding hydrophobicity around them are highly conserved, and no co-variance is detected among them in evolutionary studies.

Structures of the αI-domain on the intact αXβ2 (complement receptor 4 [CR4]) and αLβ2 (leukocyte-associated antigen-1 [LFA-1]) receptors showed a highly flexible dynamic positioning spanning a range of distances and rotations and an unprecedented partial unwinding of its α7 helix (Sen and Springer, 2016; Sen et al., 2013). This unwinding is a "shape-shifting" event that potentially equilibrates the αI-domain conformations between the closed and open states and facilitates the bidirectional allostery relay and signaling between the α/β subunits (Shimaoka et al., 2003). This exclusive crosstalk between α/β subunits at a global level, even in the absence of the external ligand, would prime the ectodomain for rapid conformational changes (Figure 1) (Sen et al., 2013), and ultimately, in the presence of dications, structural rearrangements, leading to the "maturation" of integrin affinity and signaling.

Conformational dynamism is highly expeditious for β2-integrins (~1 s) (Shamri et al., 2005), which likely confers an evolutionary advantage to leukocytes when mounting a rapid immune response. In structures of internal ligand-bound αXβ2, the αI α1 helix was captured in the "cocked" state, which shows the unique ability of the β2 I-domain to stabilize the αI-domain in the high-affinity state (Sen et al., 2013). Therein, the β2-I α1 helix is positioned in a wider groove, which helps the βI-α1 helix easily slide more than any hitherto observed motions in the β1, β3, and β7 structures; thus, this widened groove poses a state(s) to accelerate "conformational cycling" between the thermodynamically possible bent states (Figures 1A and 1F–1H), while stabilizing a long-lived, high-affinity αI-domain in the compact/bent integrin. Multiple independent studies revealed that β1-, β2-, β3-, and β5-integrins were shown to bind ligands in the compact/bent state (Azcutia et al., 2013; Bondu et al., 2017; Fan et al., 2016, 2019; Fiore et al., 2015, 2018; Saggu et al., 2018), specifically in *cis* β2-integrin interactions with the FcγIIA receptor and intercellular adhesion molecule 1 (ICAM-1) in two independent studies arrested neutrophils and limited antibody-mediated neutrophil recruitment. (Fan et al., 2019; Saggu et al., 2018) In these in *cis*-binding events, some αI-domains paradoxically seem to be stabilized in intermediate or high-affinity states, revealing the possibility that integrin could be effectively arrested in the in *cis* configuration (Figure 1F). Hence, the newly emerging conundrum is how αI-integrins avoid falling into a potential in *cis*-binding trap and achieve rapid leukocyte activation.

The MIDAS-dication assembly plays a central role in the balancing act of maintaining the aforementioned bidirectional allosteric signaling, divergent substrate recognition capabilities, and affinity maturation in αI-integrins. Dication affinities to αI-domains are reportedly weak in the mid-micromolar range (Ajroud et al., 2004; Baldwin et al., 1998; Vorup-Jensen et al., 2007). Their physiological roles in integrin functions are highly divergent, with Mg^{2+} uniformly facilitating, Ca^{2+} generally inhibiting, and Mn^{2+} universally

enhancing interactions with their cognate ligands (Dransfield et al., 1992; Leitinger et al., 2000). Particularly, the ionized Mg^{2+}—found in the range of 0.65–1.05 mM *in vivo* (Jahnen-Dechent and Ketteler, 2012)—alone mediates the transition from transient to firm adhesion and also maintains the next step, leukocyte accumulations, on the vascular surface during an inflammatory response (Sheikh and Nash, 1996). Mg^{2+}-dependent functional regulation of β2-integrins is emerging as an essential component in shaping the immune response; Mg^{2+}, by specifically modulating αLβ2 conformations and affinity, endows enhanced $CD8^{+}$ cytotoxicity against tumors and invading pathogens (Lotscher et al., 2022). Moreover, the high concentration of Ca^{2+} in the endoplasmic reticulum (ER) and Golgi mediates the folding and activation state of integrins (Tiwari et al., 2011). Despite the well-characterized impact of Mg^{2+}, Ca^{2+}, and Mn^{2+} ions on integrin functions, mechanistically how they achieve diverse and unique effects on integrin affinity regulation, allostery, and conformational changes remains to be elaborated at the molecular level.

αXβ2 and its ligand-binding domain, the αX I-domain, exhibit distinct affinity and structural changes in solution and cell surfaces, and thus, serve in our study as a receptor in characterizing the effects of dications in integrin affinity maturation and allostery establishment. αXβ2 is expressed on monocytes, tissue macrophages, natural killer (NK) cells, and most dendritic cells (DCs), and at the lower expression level on neutrophils (Hogg et al., 1986). αXβ2 modulates phagocytosis of the iC3b-opsonized particles and is known as CR4. αXβ2 has emerging unique roles, especially in regulating robust humoral responses, and its significance has been illustrated by αX-variants in autoimmune pathologies such as immunoglobulin A (IgA) nephropathy, systemic lupus erythematosus, pemphigus (blistering due to autoantibodies), and Behcet's disease (Bumiller-Bini et al., 2018; Hom et al., 2008; Kiryluk et al., 2012; Park et al., 2014). Moreover, αXβ2, via its regulator role in T cell-dependent cytotoxicity (TDCC), involves unfavorable cancer prognosis and decreased risk of death and relapse (Wang et al., 2015). Just recently, the activation of αXβ2 was shown to endow the ability of macrophages to extensively destroy malignant cells (Tang et al., 2021).

Here, we used Mg^{2+} as a fine-tuning rheostat to evolve the αX I-domain conformation in-solution between closed and open states, demonstrating the linkage between the structural dynamism and the affinity of the I-domain. This process occurred through two discerned steps with a single transition between them. In the first step, the molecular coupling is established between MIDAS and the allosteric sites—the N-terminal of the α1, α6, and α7 helices—producing the basal integrin affinity; the second step progressively enhanced the αX I-domain affinity toward the high-affinity state, and the transition period between the two steps is in the range encompassing physiological Mg^{2+} concentrations. The assembly of MIDAS-Mg^{2+}, in the first evolution phase, thrusts an unprecedented pK_a alteration of the two critical MIDAS aspartates residing in a conserved hydrophobic sink and establishes long-range molecular links between MIDAS and the αl-allosteric modules. In the second conformational evolution phase, when MIDAS inundates with Mg^{2} ions, surface plasmon resonance (SPR) and cell-based binding studies both revealed that the high-affinity state is the dominant conformation.

RESULTS

Thermodynamics of divalent cation affinity to the αX I-domain

When free of Mg^{2+}, MIDAS is occupied by two water molecules and adopts a closed state geometry (Figure 2A). The D138 rotamer pivots upon Mg^{2+}-binding, which links D138 to Mg^{2+} through invariant water coordination and stabilizes its carboxylate in the conserved “hydrophobic sink” (Figures 2B and S1C–S1E). Upon αX I-domain activation, MIDAS geometrically reconfigures itself by rearranging Mg^{2+} near T207 through a 2-Å lateral sliding of the β1α1 loop, ultimately resulting in a sandwiching of the invariant D138 and D240 between I143 and F174 (Figures 2B and 2C). To assess whether cation affinity is affected during the MIDAS reconfiguration from the cation-free/closed to the cation-bound/closed and open states, we determined the affinities and characterized the binding thermodynamics of the recombinantly expressed wild-type (WT) αX I-domain (Figure S2A, related to the STAR Methods section, expression and purification of the αX I-domain) and its high-affinity mutant to the three cations Mg^{2+}, Ca^{2+}, and Mn^{2+}. The I314G construct is locked in the alternate open/high-affinity state by isoleucine-based allosteric mutation that decouples the allostery between the MIDAS and the α7 helix (Xiong et al., 2000).

Divalent cation binding affinities to the WT αX I-domain are highest for Mn^{2+} at 69.2 μM (14,445 ± 9 M^{-1}) and Mg^{2+} at 231 μM (4,334 ± 3 M^{-1}), and weakest for Ca^{2+} at 450.5 μM (2,220 ± 8 M^{-1})(Figures 2D–2H and S2B–S2G). Mn^{2+}-binding affinity for the I314G was higher at 37.3 μM (26,485 ± 13 M^{-1}), whereas the Mg^{2+} affinity was slightly reduced to 275 μM (3,635 ± 9 M^{-1}). Binding of both Mg^{2+} and Mn^{2+} to the WT αX I-domain, as well as Mn^{2+} to the I314G, were equally driven by entropy and enthalpy. However, Mg^{2+} binding to the I314G was predominated by entropy, and the Ca^{2+} measurements were not productive (Figure 2F; Table S1). Ca^{2+} binding to the WT αX I-domain was mainly driven by entropy, suggesting an increase in structural heterogeneity and mobility at the MIDAS. While Mg^{2+} and Mn^{2+} only adopt a monodentate geometry, Ca^{2+} has unique physiochemical characteristics that enable Ca^{2+} to form bidentate ligation with either a hexa- or hepta-coordination shell (Mahalingam et al., 2011). This characteristic could be a proxy for increased conformational entropy, thereby acting as the sole modulator of the Ca^{2+}-MIDAS assembly, and a reason for its low-to-none affinity for the WT αX I-domain and I314G.

Influence of Mg^{2+} on αX I-domain stability—Mg^{2+} and Ca^{2+} are instrumental and required for αI-domain activity in extracellular space, intracellular trafficking, and secretory pathway. One proposed molecular and mechanistic interpretation of the major roles of Mg^{2+} in integrin biology is that the ion serves to establish long-range molecular interactions between MIDAS and the αI-domain scaffold. To test whether Mg^{2+} plays such a far-reaching allosteric role (rather than merely existing as a cation binding to the MIDAS), we measured the change in thermal stability of the WT αX I-domain and I314G in varying Mg^{2+} concentrations using differential scanning calorimetry (DSC). The WT αX I-domain exhibited a single cooperative unfolding transition at the melting temperature (T_m) of 53°C (Figure 3A). Stepwise Mg^{2+} titration shifted the T_m of the WT αX I-domain by 10°C–63°C and progressively increased the amplitude and area of thermograms (Figure 3A). For the

I314G, biphasic denaturation in thermograms was evident at the lowest level of bound Mg^{2+} in the presence of a smaller endotherm with a T_m of 53°C, which is greater than the major endotherm T_m of 40°C (Figure 3B). The I314G transition at T_m of 40°C also showed T_m shifting during Mg^{2+} titration from 40°C to 49°C and increased the amplitude and area of the major endotherm (Figure 3B). The minor endotherm, however, at 53°C showed Mg^{2+}-dependent T_m shifting to neither higher nor lower temperatures but gradually lost amplitude during Mg^{2+} titration (Figure 3B). The WT αX I-domain is thermodynamically more stable than the I314G, with a $\Delta\Delta H_{unfolding}$ of 34 kcal/mol and a ΔT_m of 13°C (Figures 3A and 3B).

We further assessed the Mg^{2+}-dependent stability event using an equivalent technique, differential scanning fluorimetry (DSF). T_m showed a slight or no reduction for the WT ΔX I-domain until MIDAS reached 50% Mg^{2+} occupancy (Figure 3C). However, T_m of the I314G had a well-discernible early negative slope for concentrations <82 μM Mg^{2+} (~50% MIDAS occupancy) (Figure 3D). As the MIDAS became gradually 50%–95% occupied by Mg^{2+}, the T_ms of both WT αX I-domain and the I314G increased steeply before eventually plateauing after >95% Mg^{2+} occupancy (Figures 3C and 3D).

To quantitatively analyze the bimodality of DSC and DSF thermograms, we examined the Van 't Hoff linear dependence of T_m ($1/T_m$) to the ligand concentration ($\ln[Mg^{2+}]$). Bimodality is evident in the Van 't Hoff plots of both DSF and DSC for the WT αX I-domain and in DSF for the I314G with two distinct linear relationships: one at lower (0–100 μM) and a second at higher (250 μM–250 mM) Mg^{2+} concentrations (Figures 3A, 3C, and 3D, insets). Moreover, we also modeled the Mg^{2+}-binding mode using the T_m change, which is better represented via a biphasic binding transition model for both the WT αX I-domain and the I314G (Figures 3C and 3D).

Structural consequences of Mg^{2+}-dependent ionization of two critical MIDAS aspartates—The difference in ΔT_m of 10°C and $\Delta\Delta H_{unfolding}$ of 22.9 kcal/mol between the Mg^{2+}-bound and -free states reflects a more enhanced global stability of the αX I-domain, but not the energetic contribution from the little-to-no structural rearrangements or fast-local motions within MIDAS during Mg^{2+} binding. Therefore, we characterized the physical properties of the Mg^{2+}-MIDAS assembly using cheminformatics and assessed the ionization states of the MIDAS-titratable residues using the hybrid nonequilibrium MD/Monte Carlo (neMD/MC) approach. Typically, the hydrophobic environment perturbs the pK_as of titratable acidic residues toward a neutral pH, establishing or breaking long-range global interactions as exemplified by staphylococcal nuclease and nitrophorin 4 protein. (Di Russo et al., 2012; Karp et al., 2007) Upon the addition of Mg^{2+} (+2 charge) in neMD/MC, two invariantly conserved MIDAS aspartates, D138 and D240, in the hydrophobic sink (Figures S1C–S1E) shifted their side-chain pK_a values; the shift for D138 is from 3.8 to 2.2 and the shift for D240 is from 5.9 to 3.9 (Figures 4A and 4B) at the imposed pH 7.2. Although no structural rearrangements in the MIDAS are observed during Mg^{2+} binding (Figures 2A and 2B), both carboxylates are most likely hydrated—one extra water molecule moves into MIDAS together with Mg^{2+} (Figures 1A–1C)—leading to a shift in the pK_a values of both aspartates and favoring their deprotonated charged state. At pH 7.2, the Mg^{2+}-bound closed state had steady interaction energies and stable MIDAS coordination

(Figures 2B and S3A, black trajectories; Video S1), but residues D240 and another MIDAS residue, S142, in the absence of Mg^{2+}, frequently lost the MIDAS coordination and moved out of the standard MIDAS geometry (Figures 2A and S3A, red trajectories; Video S2). Similarly, at pH 5.2, the direct interaction of D240 with S142 was also broken and replaced with a stable water molecule (Figures 2B and S3B, black trajectories; Video S3).

During transition from the closed to the open state, S142-Mg^{2+} contact coordination, which is pivotal for establishing and maintaining allosteric coupling between MIDAS and the α7 helix, stays consistently intact (Figures 2B and 2C). Moreover, during the αX I-domain opening, D240 transiently stays solvent exposed while synchronously moving with Mg^{2+} toward T207 and thus shifting its pK_a from 3.9 to 2.6 (Figures 2B, 2C and S3D). The invariant I143 moves 1 Å closer to D138 in the open state and, together with conserved F174, further creates a hydrophobic wrap around D138 (Figures S1C–S1E). This effect on the buried D138 is drastically reflected by a shift in its pK_a from 2.2 to 5.4 (Figures 2B, 2C and S3C).

Next, we tested, via proton (H^+) titration, whether the local protonation state fluctuations observed during neMD/MC affect the αX I-domain fold stability parameters (T_m and $\Delta_u G$) at different pH values using stability measurements, a widely used method to probe whether ionization of critical residues regulates global protein stability (Di Russo et al., 2012; García-Moreno et al., 1997; Karp et al., 2007). In the pH range of 3–11, the unfolding T_ms were Mg^{2+} insensitive and nearly identical (Figure 4C). Remarkably, the unfolding free energies of the αX I-domain in the pH range of 3–6 were higher by approximately 5–6 kcal/mol ($\Delta\Delta G_u$) for the Mg^{2+}-free state compared to the Mg^{2+}-bound state (Figure 4D, blue line). Above pH 6, similar unfolding free energies were followed for Mg^{2+}-free and -bound states. This observation is the most intriguing because neutral states of the critical D138 and D240 are enforced in the same pH range of 3–6 in neMD/MC, where the Mg^{2+}-free conformation showed reduced thermodynamic stability. The protonated D138 and D240 cannot bind Mg^{2+}, and the Mg^{2+}-less state, being ligand-binding incompetent, would substantially lose its ligand affinity. In fact, the previous crystallization efforts showed that the integrin αVβ3, in the pH range of 4.5–6.5, loses its dication upon crystallization (Dong et al., 2012; Xiong et al., 2009). In another study, αVβ3 affinity was reduced in response to systematic lowering of the pH (Dong et al., 2011). Since both aspartates are invariantly conserved in αI- and βI-domain MIDAS, this correlation between the ionization states of D138 and D240 and the structural stability of the αX I-domain as a function of pH appears to be inherently universal, with Mg^{2+} coupling the ionization states of both aspartates to the global stability of the αI-domain fold and subsequently establishing allostery and pH-dependent affinity.

Mg^{2+} links MIDAS to the αX I-domain fold—To identify the molecular coupling network of the Mg^{2+} ion to the αX I-domain fold, beyond D138 and D240, we performed a normal mode analysis (NMA), which maps residue-based atomic fluctuations and subsequently calculated the residue cross-correlations (RCCs) to reveal the correlated and anticorrelated regions in the αX I-domain fold (Grant et al., 2021). RCC peaks appeared between the β strands as expected since they are directly H-bonded to each other in the following order: β3–β2–β1–β4–β5–β6 (Figure 4E, green circles). Significant positive

correlations were also observed between MIDAS residue-containing β1α1-α3α4-α4β4 loops (Figure 4E, red circles). A direct long-range coupling exists between the α7 and α1 helices, the latter of which is immediately preceded by MIDAS (Figure 4E, blue circle). In fact, a recent mutational study on the α1 helix confirmed the universal role of both helices regulating the MIDAS affinity (Wang et al., 2017). The second long-range route between MIDAS and the α7 helix propagates among the loops holding the cation in place (Figure 4E, red circles); the α7 helix and the β6α7 loop, both of which cooperatively regulate ligand affinity, are directly coupled to the β5α6 loop. The β5α6 loop is linked to both the α3α4 loop containing T207 and the β1α1 loop containing the key MIDAS DXSXS motif (Figure 4E, black/green dashed lines). The α3α4 loop also shows a second strong correlation with the β4α5 loop that bears the key residue D240. Through a subglobal structural rearrangement in MIDAS—the lateral motion of Mg^{2+} and the β1α1 loop by 2 Å and D138 rotamer flip—D240 loses its direct Mg^{2+} coordination to T207 during αX I-domain opening (Figure 2C).

We further assessed the local molecular breathing in the Mg^{2+}-free and -bound states using the dynamic RCC (dRCC) matrices extracted from neMD/MC simulations. Trajectories in pH evolution during our neMD/MC simulations account for the ionization states of residues, and dynamic cross-correlation (DCCM) of these trajectories best represent harmonic vibrations that reveal a major aspect of the "breathing" motions within the αX I-domain fold. The principle of minimal frustration (Bryngelson and Wolynes, 1987), a term defined as a general feature of a model Hamiltonian to describe protein foldedness, infers the reduction of strong energetic conflicts in a protein fold, or more precisely, the bringing together of residues in space with thermodynamic stabilization of the protein fold. Thermodynamic stabilization comes with minimal frustration, and in comparison to the unfolded state, reduces excessive breathing motions and random residue correlation toward a unique structural ensemble(s), creating a tunable conformational landscape, and eliciting allosteric modulation. In the Mg^{2+}-free state, we observed a scattered, non-specifically intense, and extensive dRCC matrix, suggesting high energy and maximum frustration (Figure S3F, related to Figure 4E). Mg^{2+} binding dampened excessive residue cross-correlation contacts, minimizing frustration with precise interactions unique to the αX I-domain scaffold similar to the static RCC (Figure S3E, related to Figure 4E). This difference is evident and presented in the difference DCCM map (Figure S3G, related to Figure 4E). In short, reduced breathing motion or minimal interaction frustration conferred by Mg^{2+} binding is accompanied by an increase in the structural stability of the αX I-domain scaffold, suggesting that the Mg^{2+}-MIDAS assembly is thermodynamically more stable, and thus, has established an allostery among structural elements of the αX I-domain.

Mg^{2+} induces bimodal shape-shifting on the αX I-domain—Mg^{2+} binding in-solution also alters the secondary structure content of the αX I-domain as probed by circular dichroism (CD) (Figures S4A–S4C, related to Figure 5D). To directly visualize the ensemble-averaged conformational changes, we simultaneously collected small and wide-angle X-ray scattering (SWAXS) intensities for the αX I-domain in varying Mg^{2+} concentrations. The positive slope seen in intensity profiles of the αX I-domain scattering with increasing levels of free Mg^{2+} from 0 to 100 mM is indicative of the αX I-

domain becoming enlarged (Figure 5A). Indirect Fourier transformation of intensities of each SWAXS dataset, q ranges between 0.015 and 1 $Å^{-1}$ (Table S2), in varying Mg^{2+} concentrations were used to estimate the pairwise distance distribution curves (P(r)) of the scattering vectors. The three-dimensional (3D) plot of P(r) versus particle radius r(Å) in varying Mg^{2+} concentrations (Figure 5B) revealed a stepwise evolution of effective radius (D_{max}) and radius of gyration (R_g) of the αX I-domain, extending its D_{max} from 50 to 78 Å and R_g from 18.2 Å to 29.5 Å (Table S2). The 3D plot also displayed two distinct D_{max} evolution times that are inosculated with a transition plateau phase between them. The first evolution time exists in partially occupied MIDAS, corresponding to <0.5 mM Mg^{2+}, and exhibits a more compact shape. Next, a plateau region appears in which D_{max} and R_g stay unchanged in the range of 0.5–5 mM Mg^{2+} while Mg^{2+} concentrations above 5 mM initiated the second D_{max} evolution time in solution (Figure 5B). The comparable I_0/c values, the linear Guinier regions, and dimensionless Kratky plots of X-ray scattering showed that changes in the αX I-domain shape are a direct consequence of alterations in macromolecular dimensions and not intermolecular aggregation (Figures S4E and S4F, related to Figures 5A and 5B).

The concentration range where D_{max} plateaued appears to be a conformational transition zone and interestingly corresponds to the physiological Mg^{2+} concentration. That is, this mid-zone is potentially populated by diverse conformational states in solution. If so, we predict that the mid-plateau Mg^{2+} concentration of 1 mM could serve as the slow exchange regime in the NMR time-scale ($conformational_{\text{equilibrium}} << \backslash\Delta\nu_{the\ chemical\ shift\ difference}|$) and allow us to define residues that could adopt one (stable) or multiple (dynamic) conformations. The 3D-HNCACB/HN(CO)CACB NMR datasets were collected using a $^{2}D/^{15}N/^{13}C$ isotopically labeled αX I-domain in 1 mM Mg^{2+}. During the backbone chemical shifts assignment, a set of resonances (peak splitting) for both Cα (red peaks) and Cβ (green peaks) were detected showing configurational interconversion during the frequency detection period (Figures 5C and S5). That is, at least two structural states clearly existed in mid-plateau Mg^{2+} concentration. Residues that showed peak splitting were mapped onto the superimposed closed and open αX I-domain structures. For simplicity in Figure 5D, the superimposed closed and open structures are colored by root-mean-square deviation (RMSD), and the Cα atoms of residues that undergo peak splitting are shown as spheres. Residues adopting at least two configurational states were remarkably localized to the allosteric regions—the N-terminal half of the α1 and α6 helices, the entire α7 helix, MIDAS, and loops in the close vicinity of MIDAS—that undergo structural alteration during the αX I-domain opening. Cα-RMSDs of residues between the closed and open states, which either exhibit peak splitting or show single resonance, are 9 and 0.8 Å, respectively (Figures 5D and S4H). Furthermore, the residue-based in-solution dynamism probed by NMR is also noted in Figure 4E (yellow-shaded strips) showing similar RCCs for the residues with peak splitting. Briefly, these dynamic residues probed by NMR and RCC are highly comparable and potentially play a major role in establishing the molecular coupling of MIDAS to the αI-domain scaffold upon Mg^{2+} binding.

Effects of increasing Mg^{2+} concentration on the MIDAS-dependent αX I-domain affinity—Do Mg^{2+}-induced structural changes observed in solution enforce any

functional regulation onto the integrin external ligand affinity? To examine αX I-domain adhesiveness in varying Mg^{2+} concentrations to its physiological ligand, fibrinogen, we characterize their affinity evolution using SPR. We analyzed our SPR binding traces using maximum entropy or Tikhonov regularization, which accounts for heterogeneous interactions (e.g., structural interconversion and surface heterogeneity) and returns 3D-dimensional coordinates, with a range of the K_d (in micromoles) and k_{off} (in 1/s) on the x-y axis and the abundance or multiplicity of the probed interaction(s) in the z coordinates, as a contour map (Gorshkova et al., 2008). Interactions of the WT αX I-domain and the I314G with fibrinogen-coated surfaces produced robust SPR signals in the presence of 0.1, 0.5, 5, 10, and 50 mM Mg^{2+} with 2D-grid points set to the range of K_d and k_{off} from 10^{-9} to 10^{-2} μM and 10^{-9} to 1 s^{-1}, respectively.

The binding to fibrinogen in 0.1 mM and 0.5 mM Mg^{2+} showed an affinity centered around a K_d of 80×10^{-5} M and another minor affinity population around $K_d = 1 \times 10^{-5}$ M. This small population of the high-affinity αX I domain at physiological relevant concentrations of Mg^{2+} provides *in-solution* evidence indicating that a mixed ensemble of αX I-domain conformations exists (Figures 6A and 6B). Here, the affinity of the minor population is similar to the affinity of the I314G. Increasing Mg^{2+} concentration progressively shifted the center of the K_d peak toward a high-affinity state (Figures 6A–6E; Table S3) while reducing the heterogeneity of the major conformational ensemble on the K_d/K_{off} matrix as shown by reduced dispersity of the 2D-binding sensorgram (Figures 6A–6E and S6A). At 10 mM and 50 mM Mg^{2+}, the affinity was fully matured to the high-affinity of K_d of 2×10^{-5} M (Figures 6D and 6E, Table S3) and structural heterogeneity reduced to a minimum (Figures 6E and S6A). Nevertheless, the stepwise increase in Mg^{2+} concentration neither induced a similar stepwise affinity maturation of the I314G nor shrunk the 2D space of the K_d/K_{off} binding matrix, confirming that the I314G is locked in the alternate high-affinity state (Figures 6F–6J and S6A). The observed affinity of the I314G to fibrinogen is ~100 μM for each of the five Mg^{2+} concentrations, which is equivalent to the K_d of the fully affinity-matured WT αX I-domain (Figures 6E versus 6F–6J).

Mg^{2+}-induced affinity maturation of intact αXβ2 integrin on cell surfaces—

Next, we tested the functional relevance of the Mg^{2+}-dependent affinity increase in the αX I-domain on cell surfaces. αXβ2 is known as CR4 and is one of the essential components of innate immunity that phagocytizes complement-opsonized particles or complexes. iC3b rosetting that mimics the first step of this phagocytosis is widely used, physiologically relevant in immunological assays in which αXβ2-expressing target cells form aggregates with ligand-coated (iC3b-sensitized) erythrocytes (Figure S7A, related to the STAR Methods section “E-IgM-iC3b rosetting assay”). However, assessing the cation-dependent αX I-domain affinity on cell surfaces (as in the intact αXβ2 receptor) is challenging due to the bilateral regulatory roles of cations in modulating the affinities of both the αX and β2 I-domains. In detail, the cation-modulated affinity events that simultaneously occur and are collectively reflected in the αX I-domain affinity could be split into two major interactions: (1) the binding interaction of the external ligand to the αX I-domain that we want to quantify in response to increasing Mg^{2+} and (2) the internal ligand binding (interactions of the αX/β2 I-domains) that indirectly tunes the external ligand binding (Figure 1E, red

arrow). To exclude the second effect in our binding assay, we locked the β2 I-domain into the internal ligand binding-incompetent state using either inhibitory monoclonal antibody (mAb), TS1/18, or small-molecule inhibitor XVA143. The allosteric inhibitor, XVA143, patented by Roche (Yang et al., 2006), directly competes with the αI-α7 helix binding at the β2 I-MIDAS efficiently with an half-maximal inhibitory concentration (IC_{50}) of 60 ± 1 nM. TS1/18 binds to an epitope on the β2 I-domain (R133 and Q332) and locks the β2 I-domain MIDAS into the closed state (Lu et al., 2001). Both XVA143 and TS1/18 inhibits the allosteric crosstalk between the β2 and αX subunits. Also, their epitopes are not in close vicinity to the αX I-domain—81 and 63 Å away from its MIDAS, respectively. Thus, they would not directly affect the αX I-domain conformation and affinity state. In our assay, Mn^{2+} acts as the universal integrin activator that replaces ADMIDAS Ca^{2+} and was previously shown to allosterically increase αI-domain affinity (Dransfield et al., 1992). Since both allosteric inhibitors TS1/18 and XVA148 could block the Mn^{2+}-dependent β2 I-domain activation, the Mn^{2+}-effect on the αX I-domain could be uniquely probed in our binding assay.

In 1 mM Mn^{2+}/Ca^{2+}, αXβ2 showed high affinity because Mn^{2+} stabilizes the open/active βI-domain and induces internal ligand binding, hence transducing allostery relay and substantially increasing the αI-domain affinity (Figure 6L, yellow area). This Mn^{2+}-induced iC3b rosetting is well inhibited upon the addition of TS1/18 (in a dose-dependent manner) (IC_{50} = 6.8 μg/mL)(Figure 6K) or XVA143 (Figure 6L, yellow-shaded area), demonstrating that both inhibitors disengage the βI-domain from the α/β crosstalk and provide strategies to assess the direct role of Mg^{2+} on the αX I-domain affinity on cell surfaces. Both 1 μM XVA143 and 10 μg/mL TS1/18 are sufficient to inhibit the αXβ2 affinity level similar to that of the un-opsonized erythrocytes.

Next, we examined how Mg^{2+} ion concentration directly influences αX I-domain adhesiveness on the intact integrin. Overall, a stepwise increase in Mg^{2+} concentration to 100 mM in 1 mM Ca^{2+} greatly enhanced iC3b rosetting of αXβ2 (Figures 6L, blue line, and S7B). Since both βI- and αI-domains have MIDAS, the increased iC3b rosetting observed could be induced by Mg^{2+} binding to either domain. Next, we used TS1/18 and XVA143 to block β2-ί MIDAS activation; any affinity change then becomes independent of the β2 I-domain and only stays dependent on the αX I-domain affinity maturation. In higher concentrations of Mg^{2+}, incubation of αXβ2-expressing cells in the presence of TS1/18 and XVA143 still exhibited enhanced binding (Figure 6L, red/green dashed lines), directly showing that the increased affinity only corresponds to the Mg^{2+}-induced αX I-domain opening. In short, both of our *in vitro* SPR and cell-based affinity measurements showed that the αX I-domain, in the absence of help from the β2 I-domain, could mature its affinity in ranges of Mg^{2+}-ion concentration above 5 mM, which corresponds to the Mg^{2+} effect observed as the second conformational evolution step in our small-angle X-ray scattering (SAXS) data.

DISCUSSION

Cation-αX I-domain affinities (K_a) probed in our study are weak in a measurable range and on the order of Mn^{2+} > Mg^{2+} > Ca^{2+}. These measurements agree well with the absolute

binding free-energy calculations determined for the αL and αX I-domains (data not shown) and the experimental measurements for αL and αM I-domains (Baldwin et al., 1998; San Sebastian et al., 2006; Vorup-Jensen et al., 2007). We also extracted the thermodynamic parameters of cation-binding events. Although not drastic, systemic alteration of divalent cation affinity was observed and TΔS (entropy) was more pronounced for the I314G in binding of Mg^{2+} and Mn^{2+} (Table S1). This observation is supported by the structural rationale for the engineered activation mechanism of I314G, which (1) loosens the α7 helix interaction with the rest of the αX I-domain fold and (2) reduces its helical propensity (helical propensity scale of Ile and Gly are 0.41 and 1, respectively, with 0 being the most, and 1 the least, favored), which, in turn, triggers a concurrent unwinding of the α7 helix. These subglobal structural changes in the I314G, together with the swap of the charged to non-aqueous $M(g/n)^{2+}$ coordination in the primary coordination sphere (D240 to T207, Figures 1B and 1C), potentially make the MIDAS-$M(g/n)^{2+}$ complex and αX I-domain structure more labile, accounting for the enhanced conformational entropy observed during the binding of Mg^{2+} and Mn^{2+} ions.

The observed thermodynamics differences in our isothermal titration calorimetry (ITC) analysis between Ca^{2+}, Mg^{2+}, and Mn^{2+} also would result from differences in their physicochemical properties. In general, the binding enthalpy describes the favorability of the molecular interactions via hydrophilic, H-bonding, electrostatic interactions, and conformational changes of interacting molecules while the binding entropy arises from restructuring water and ions and hydrophobic effects (Dutta et al., 2015). Interestingly, the detected binding enthalpy of the Ca^{2+} to MIDAS in our titrations and previous studies (Ajroud et al., 2004; Vorup-Jensen et al., 2007) is marginal, and Ca^{2+} affinity is almost completely driven by temperature-dependent entropy rather than enthalpy (Table S1). Given that Ca^{2+} has a low electronegativity (Pauling unit of 1) and could interconvert between monodentate and bidentate geometries, its ionic tethering and assembly to MIDAS by the electrostatic Ca^{2+} steering or molecular diffusion is potentially less effective in comparison to ionic tethering of Mg^{2+} and Mn^{2+} (Pauling units of 1.31 and 1.55, respectively). Consequently, the Ca^{2+}-MIDAS assembly is loosely established and, hence, explains the almost negligible Ca^{2+}-binding enthalpy. In our QM calculations, the absolute binding energy of Ca^{2+} relative to that of Mg^{2+} and Mn^{2+} in both a vacuum and in water is lower (data not shown). In fact, the observed Ca^{2+}-MIDAS assemblies in integrins display loose tethering, which is highlighted by heterogenic or polygonal (hexa- or hepta-) coordination in the complex formation of the αI-domain with a ligand mimetic antibody (mAb107) and also in other proteins (Mahalingam et al., 2011; Nayal and Di Cera, 1994; Schymkowitz et al., 2005). Aside from electronegativity, the ionic radii of Ca^{2+}, Mg^{2+}, and Mn^{2+} are also different: 1.14, 0.86, and 0.81 Å, respectively. Ca^{2+} has the largest ionic radius and thus larger van der Waals (Shannon, 1976). The effect of varying size would also partially contribute to the difference in cation affinities and binding thermodynamics due to the formation of different electrostatic networks and water solvation around MIDAS.

Roles of cations in integrin biosynthesis are essential; Ca^{2+} concentration in the ER and Golgi apparatus ranges at ~3 mM in the steady state and helps the folding of the integrin receptors (Montero et al., 1995). The dampening of integrin promiscuity by the Ca^{2+} effect would keep the integrin in the bent and binding-incompetent state in the intracellular

space (Tiwari et al., 2011), concomitantly blocking any potential in *cis* interactions during integrin biosynthesis and folding in ER and Golgi. This could be highly critical during the biosynthesis of αXβ2 and its sister homologs αMα2 and αDα2 since they are famous for being extensively promiscuous, recognizing structurally dissimilar biomolecules ranging from proteins to nucleic acids (Vorup-Jensen and Jensen, 2018).

The hydrophobic residues in the immediate 5-Å vicinity of D138 and D240 envelop aspartates better in the closed MIDAS configuration and favors the neutral and Mg^{2+}-free state of both D138 and D240 by increasing their pK_as by forming an enlarged hydrophobic sink around them by 270 $Å^2$ (Figures S1D–S1C). This prominent hydrophobicity would create an inhibitory effect on the Mg^{2+}-dependent ligand binding as demonstrated by mutational studies in literature. Reducing the local hydrophobicity via αL-F292A or αL-F292G mutations (F300 is the corresponding residue in the αX I-domain) increased the affinity by 75- and 12,000-fold (Jin et al., 2006). However, the energetic penalty for swapping Ala to Gly (methyl to proton mutation) in the position of the conserved αL-F292 would theoretically lead to an affinity increase by only 3-fold. It is, thus, tempting to speculate that the 160-fold (12,000/75)—not the 3-fold—affinity increase observed between Ala and Gly mutants stems from the difference in the considerable side-chain hydrophobicity index (Δt_R) of 41 between Ala and Gly, creating this large affinity gap (Monera et al., 1995).

The ionization states of two MIDAS aspartates, D138 and D240, in the absence of Mg^{2+} in our neMD/MC (Figures 4A and 4B), showed markedly elevated pK_as identified relative to the average intrinsic pK_a for Asp residues in proteins (Grimsley et al., 2009). The local dielectric constants for both aspartates, relative to the reference ionization state, were calculated using the Born equation as described in the Method details section. In the absence of divalent cations, D138 and D240 (ε_{D138} = 24.7 and ε_{D240} = 20.9, ε_{H_2O} = 78.3) experience a less polarizable environment. In general, this low dielectric effect, while sequestering apolar residues as clusters, promotes neutral states of polar residues and tethers them in a semi-rigid or high configuration entropy (García-Moreno et al., 1997). Hence, the differential permittivity shift around both aspartates help accommodate the counter negative charge for Mg^{2+} when the ion is present or adopt a neutral/protonated configuration in the absence of Mg^{2+}. What is unique about this permittivity shift at the immediate vicinity of both aspartates is that, with the αX I-domain, we have detected here that the changes in conformational reorganization/equilibria (SAXS), long-range residue coupling, and stability of the αI-domain (DSC/DSF) are concomitant with the ionization states of both aspartates. This observation most likely deciphers the importance of pK_a changes of the invariant aspartates in regulating the integrin affinity during endosomal transport.

Our binding studies both *in vitro* and on cell surfaces showed that αXβ2 adhesiveness could be fine-tuned in response to shifting Mg^{2+}-ion concentration, and the resultant affinity maturation shaped more homogeneous interactions between the αX I-domain and its ligands. During affinity maturation, the k_{off} rate was not altered, but the ligand affinity (K_d) and k_{on} rates were enhanced in response to the increasing Mg^{2+} concentration. Two potential mechanisms could implicitly define the Mg^{2+}-mediated k_{on} increase—the enriched molecular steering of ligands or/and the induction of a vast αX I-domain conformational

landscape. Since all integrin ligands bind through either an Asp or Glu to the αI-domains, the first mechanism is plausible in that Mg^{2+}-ion residency in MIDAS favorably develops ligand steering and has a direct role in k_{on}. In the second mechanism, the assembly of the Mg^{2+}-MIDAS complex is mainly controlled by binding entropy for the I314G, but equally controlled by both binding entropy and enthalpy for the WT αX I-domain. These observations also suggest that greater conformational space between the ligand-free and ligand-binding competent conformations is explored in the open state and that the second structural evolution induced by Mg^{2+} concertation above 5 mM would probably create a more labile MIDAS, contributing partly to the increase in k_{on}. In other words, since the binding-competent geometry or geometries between the ligand and the αX I-domain are enriched toward a unique interface, the equilibration time needed for disassociation of the very same interface (k_{off}) would not be dependent on the free Mg^{2+} concentration, and this is why k_{off} most likely remained unaltered in our SPR-Mg^{2+} titrations.

What is the basis of the molecular mechanism that facilitates ligand binding in the extracellular space and separates the integrin-ligand complex during the endocytic stage after receptor internalization? pH at the extracellular space, ~7.4, supports the external ligand binding. However, the integrin-ligand complexes, after receptor internalization, face progressive acidification in their journey from the early to late endosome from pH of 6.5 to 5 (Caswell et al., 2009; Kharitidi et al., 2015; Piper et al., 2014; Rabb et al., 1993). Potential protonation of MIDAS aspartates in the endocytic compartments would disfavor Mg^{2+} accommodation in MIDAS and subsequently dissociate the integrin-ligand complex. This scenario is supported by a sharp decline in the external ligand affinity *in vitro* affinity assays and the lack of a MIDAS cation in crystal lattices in the reduced pH of 5 (Dong et al., 2012, 2014). Perhaps most remarkably, this pH dependence of the MIDAS-ionization state would favorably regulate dissociation of the integrin-ligand complex during endosomal transport and aid the integrin-recycling mechanism.

The Mg^{2+}-ion concentration that supports integrin binding to physiological ligands in blood is in the range of 0.65–1.05 mM (Jahnen-Dechent and Ketteler, 2012). We artificially used a range of Mg^{2+}-ion concentrations outside of this physiological range (>5 mM), which led to the enlargement of its effective radius. Non-physiological, high Mg^{2+} concentrations in our assays could be considered as a proxy for the force-mediated αX I-domain activation. Interestingly, the force-induced enlargement of the αI-domain and an immediate increase in its ligand binding were previously observed (Fu et al., 2015). Hence, a range of Mg^{2+}-ion concentrations outside of the physiological range served to progressively bring forth the spectrum of structural states that rarely exist under basal conditions on cell surfaces but are frequently visited under force. The Mg^{2+}-induced conformational dynamics observed herein provide a structural pathway that demonstrates the skewed affinity of Mg^{2+} for the open compared to the closed MIDAS configuration. In the presence of overexpressed ligands (e.g., ICAM-1, VCAM-1 [vascular cell adhesion protein 1] on the inflamed tissue or atherosclerotic plaque), the biased conformational equilibrium toward the high-affinity state would thermodynamically drive the assembly of both in *cis* and *trans* integrin-ligand complexes (transition from Figures 1G–1E or 1H), even when MIDAS is not fully saturated on cell surfaces.

Another striking observation in our cell-affinity assays is that Mn^{2+} increases αI-integrin's affinity by promoting internal ligand, not external ligand, binding and directly transitioning the β2 I-domain to the active state. TS1/18 or XVA148 dampened the Mn^{2+}-dependent β2 I-domain activation, thus allosterically inhibiting the external ligand binding. Indeed, supporting evidence was previously observed: Mn^{2+} did not increase the binding affinity of the α2 and αX I-domains to collagen and plasminogen in the equimolar concentrations of Mg^{2+} (Calderwood et al., 1997; Gang et al., 2007), suggesting that universal Mn^{2+}-dependent integrin activation must originate from the activating Mn^{2+} effect on the β2 I-domain, potentially replacing the ADMIDAS Ca^{2+} with Mn^{2+}.

Mg^{2+}-dependent progressive enlargement in the molecular shape of the αX I-domain, and its initial (Mg^{2+} free) and final (100 mM Mg^{2+}) envelope radii are consistent with the effective radius change observed in the X-ray structures (Sen and Springer, 2016; Sen et al., 2013). Although it is impossible to assign which particular secondary structure(s) drives the Mg^{2+}-dependent radius evolution of the αX I-domain based on the shape of scattering, extension (at the scale of 28 Å) in a globular Rossman fold is theoretically plausible if and only if either the N or C terminus outspreads. Structural consequences of the in-solution enlargement, including differential ionization of aspartates, allostery establishment, and positional changes in the α1, α6, and α7 helices, bring about a high degree of conformational freedom of the αX I-domain fold, relative to the remainder of the αXα2 protein, and obviate the geometric constraint of the αX I-domain/ligand assembly. In previous crystallization trials, the αX I-domain was detected in two different orientations on three αXα2 ectodomain structures and were missing in two other αXα2 crystals (Sen and Springer, 2016; Xie et al., 2010). Lack of the αX I-domain in the latter structures potentially resulted from the averaging out of the αX I-domain electron density in the data noise due to its high positional flexibility in these lattices. Moreover, sister αI domains were shown to rotate and tilt above the platform formed by the β propeller and βI domains; the αL, αM, and αX I-domain orientations on ectodomains and headpieces differ by 150° (Jensen et al., 2021; Sen and Springer, 2016; Sen et al., 2013; Sen et al., 2018). The global flexibility of the αI-domain fold, relative to the remainder of the integrin, appears to be a natural consequence of the intrinsic dynamics within the αI-domain scaffold probed here.

Our findings here provide an important mechanistic insight into the regulation of leukocyte function via the Mg^{2+} ion in both adaptive and innate responses. It was recently shown that Mg^{2+} concentration dictates $CD8^+$ T cell cytotoxicity in the cancer microenvironment by tuning the αLβ2 conformational equilibrium and affinity, and the activation of αXβ2 has been directly linked to the unprecedented ability of monocyte-derived inflammatory cells to phagocytose malignant cells (Lotscher et al., 2022; Tang et al., 2021). Hypomagnesemia has been, however, linked to impaired immune response against influenza virus, osteoporosis, stroke, cardiovascular and diabetic pathologies, worse outcomes in cancer immunotherapy, and infection (Adebamowo et al., 2015; Castiglioni et al., 2013; Kanellopoulou et al., 2019; Saris et al., 2000; Zhao et al., 2019, 2020). Moreover, the physiological Mg^{2+} concentration must be maintained to transition neutrophils from the integrin-dependent rolling to the firm adhesion state (Sheikh and Nash, 1996), a critical step in leukocyte trafficking. It is most interesting that physiological Mg^{2+} concentration is the "splitting point" of the integrin-dependent affinity maturation observed here, which critically transforms leukocyte

behavior in the aforementioned literature. Simply put, the immediacy of Mg^{2+}-dependent regulation on leukocyte function reveals the metal-ion sensitivity of the β2-integrins as a potential modulator in autoimmune pathologies and cancer and has translation potential. Further studies *in vivo* are needed to define the functional coupling between the Mg^{2+} ion and the α2-integrin receptors.

The dynamic continuum that was prominently observed as two evolution periods in our study using differential Mg^{2+} concentration yielded unexpected discoveries. First, differential ionizations of MIDAS aspartate residues that are instigated upon dication binding enable the integration of long-range coupling between allosteric components of the αX I-domain. Second, saturation of MIDAS with Mg^{2+} ion helps increase the αX I-domain affinity by exploring a more extended, hitherto unexplored heterogeneous, conformational space, which could be specialized not only to mediate ligand recognition but also to simulate intermediate/transitionary states between closed and open αX I-domain states. This rapid equilibration between the binding-competent and -incompetent states could have two different functional outcomes: (1) it helps the integrin readily engage to the ligand either upon inside-out signaling or when the ligand is overpresented or (2) it thwarts the leukocyte integrin from being arrested into an inexorably locked in *cis* bound configuration via conformational cycling (Figure 1). Thus, both scenarios would enable a rapid dynamic continuum between the bent and extended states on cell surfaces.

Limitations of the study

We show here that Mg^{2+} potentially primes αX I-domain conformational changes. Conversely, the Ca^{2+} effect and the interplay between these two physiologically abundant cations would not apply. This limitation, therefore, points toward future work on the mechanistic connection between cation-dependent events that would extend the current understanding of the physical foundation of integrin-cation biology.

STAR★METHODS

RESOURCE AVAILABILITY

Lead contact—Further information and requests should be directed to and will be fulfilled by the lead contact, Mehmet Sen (msen2@cougarnet.uh.edu).

Materials availability—This study did not generate any new, unique reagents.

Data and code availability—All data reported in this paper will be shared by the lead contact upon request. This paper does not report original code. Any additional information required to reanalyze the data reported in this paper is available from the lead contact upon request.

EXPERIMENTAL MODEL AND SUBJECT DETAILS

This study has used the following cell lines: HEK293T cells (ATCC; Cat# CRL-3216) and *E. coli* Rosetta BL21 (DE3) cells (EMD Millipore; Cat# 70954-3). All HEK293T cells were grown following the standard protocols. Briefly, they were grown in DMEM (Gibco

Cat#10313), Pen Strep (Gibco Cat# 15140-122), and 10% FBS at 37°C with 5% CO_2 in T-Flasks or plates. For culturing *E. coli,* general LB media, carbenicillin, chloramphenicol, and IPTG (Goldbio; Cat# C-103-5, C-105-5, and I248100) were used at 37°C at 225 rpm in a shaker incubator.

METHOD DETAILS

Expression and purification of the αX I-domain—The human αX I-domain (residues Q129 to G319) and the I314G construct were cloned into pgEX-6P and expressed in *E. coli* Rosetta BL21 (DE3) cells. Cells inoculated from the overnight starting culture were grown in Luria-Bertani (LB) media containing 100 μg/mL carbenicillin and 100 μg/mL chloramphenicol at 37°C at 225 rpm until an OD_{600nm} of 0.5–0.7 was reached. The culture was cooled to ambient temperature, induced with 1 mM isopropyl-1-thio-B-D-galactopyranoside (IPTG), and then incubated overnight (14–16 hours) at 22°C at 225 rpm. Cell pellets were re-suspended in lysis buffer (20 mM Tris-HCl, 200 mM NaCl, 10% glycerol, pH 8.0) and thoroughly lysed by passing the cell suspension through an Avestin EmulsiFlex C3 homogenizer at 10,000 psi five times. The cell lysate was incubated with 1X phenylmethanesulfonylfluoride (PMSF) and 1 mM DNase by gently rocking at 4°C for 30 minutes followed by centrifugation at 20,000 X *g* in polycarbonate centrifuge tubes for 30 minutes at 4°C. The filtered supernatant was loaded onto a Glutathione Sepharose (GST) column. The recombinant protein was eluted in elution buffer (20 mM Tris-HCl, 200 mM NaCl, 10 mM reduced glutathione, 10% glycerol, pH 8) and digested with human rhinovirus 3C Protease at a ratio of 1:20 protease:protein for 16 hours at 4°C for complete digestion. The digestion mixture was spun down to remove possible precipitation and the resulting supernatant was passed through a Ni-Sepharose HisTrap HP column to remove the his-tagged 3C protease. The collected flow-through was further passed onto the equilibrated GST column to remove the cleaved GST protein. The resulting flow-through was the 22 kDa αX I-domain. Finally, the concentrated sample was further purified on a 16/60 Superdex 75 size-exclusion chromatography column in polyvalent cation-free buffer containing 20 mM HEPES, 150 mM NaCl, pH 7.5. The purification procedures eventually yielded 5–7 mg of the monomeric αX I-domain with approximately 95% purity from 1 L of bacterial cell culture (Figure S2A). The protein concentration was measured by its absorbance at 280 nm using the native extinction coefficient of 11470 $M^{-1}{\cdot}cm^{-1}$. The native extinction coefficient of the αX I-domain was calculated by BCA assay.

Isothermal titration calorimetry (ITC)—100 μM WT αX I-domain or 50 μM I314G construct were loaded into MicroCalorimeter PEAQ-ITC with a cell volume of 200 μL in buffer containing 20 mM Tris, 150 mM NaCl, pH 7.5. For the WT αX I-domain titrations, 7.5 mM Mg^{2+}, 4 mM Mn^{2+}, and 20 mM Ca^{2+} in identical buffer were injected for 38 cycles in volume of 0.5 μL and 1 μL in the rest of the titration with continuous stirring at 25°C. For the I314G construct, 3.7 mM Mg^{2+} and 2 mM Mn^{2+} were titrated with the same injection protocol used for the WT αX I-domain. Binding enthalpy (ΔH^0)(kcal/mol) versus the molar ratio of cation to the αX I-domain was generated from each injection, and then the resulting isotherm was deconvoluted to calculate cation affinities and energetics. Calorimetry titration curves were fitted using Bayesian Markov Chain Monte Carlo (MCMC) methods (Duvvuri

et al., 2018), yielding the 2D-correlation map of the binding constant (K_a) and enthalpy ($\Delta H^0_{binding}$)(Figures 2D–2H and S2B–S2G).

Differential scanning calorimetry (DSC)—Immediately before the experiment, Mg^{2+} at different concentrations was mixed with 45.5 μM of the WT αX I-domain and I314G construct and placed on auto sampler 96 well plate in MicroCal PEAQ-DSC at 4°C. The experiment was performed at a temperature range spanning from 15°C to 70°C and at the scan rate of 60°C per hour in the passive feedback mode. A 10-minute pre-scan thermostat mode was considered for the baseline equilibration. Data were analyzed using PEAQ-DSC software which included buffer subtraction from protein sample scan, baseline subtraction of heat capacity difference between baselines of pre-transition and post-transition, and concentration normalization.

Differential scanning fluorimetry (DSF)—A thermal shift assay via differential scanning fluorimetry (DSF) was used to characterize the stability of the αX I-domain in varying Mg^{2+}-concentrations and pH range of 3–11. Prior to setting up the reaction in the 96-well plate, a master reaction mix including the 5 μg αX I-domain, 10X Sypro Orange dye, and the buffer (20 mM HEPES, 150 mM NaCl, pH 7.5 in metal-free water), was prepared. Different stock concentrations of the Mg^{2+} were prepared and subsequently added to each well. Each Mg^{2+}concentration was prepared in at least triplicates, noted as black dots with standard deviation shown as bars (Figures 3C and 3D). The total reaction volume per well in the PCR plate was 20 μL. The reaction mixture with the αX I-domain, Sypro Orange, and buffer in the absence of cations was the positive control, and the negative control included a mixture with the αX I-domain and buffer without the Sypro Orange. The fluorescence was measured at regular intervals with the temperature gradient of 0.1°C per 15 seconds over a temperature range spanning from 15°C to 95°C in the CFX96 real-time PCR instrument (Bio-Rad). We tested by DSF titration curves whether are mono-phasic or biphasic (Figures 3C and 3D). Differential change in the melting profiles of the WT αX I-domain and I314G construct showed bi-phasic Mg^{2+}-binding characteristics in Mg^{2+} concentrations ranging from 1 μM to 100 mM. For statistical rigor, we compared the bi-phasic (red-line) and mono-phasic fit (blue-line) binding profiles for both the WT and I314G construct using *F*-tests (Figures 3C and 3D). p-values of 0.0068 and <0.0001, respectively, strongly confirm bi-phasic transition. For experimental rigor, we checked whether the observed melting temperature (T_m) changes resulted from the Hofmeister or lyotropic effect or the gradual increase of the ionic strength but found that such an increase did not alter T_m of the αX-I domain (Figure S2H, related to the STAR methods section, differential scanning calorimetry).

The Van 't Hoff linear dependence of T_m ($1/T_m$) to the ligand concentration ($\ln[Mg^{2+}]$) was calculated for our DSC and DSF data with the following equation; (Shrake and Ross, 1988),

$$\Delta H_{Van'tHoff} = nRT\ ln\ ln\left(Mg^{2+}\right)_0 + c\ \# \qquad \text{(Equation 1)}$$

where $\Delta H_{Van'tHoff}$ is the temperature-independent enthalpy of the αX I-domain unfolding, R is the gas constant, T is the temperature (Kelvin), n is the number of binding sites ($n = 1$ for Mg^{2+}), and c is constant.

Nonequilibrium MD/Monte Carlo (neMD/MC)—The hybrid nonequilibrium MD/Monte Carlo (neMD/MC) approach, a type of constant-pH MD simulation, was used to predict the pK_a of Asp 138 and 240 (Chen and Roux, 2015). A total of three systems were set up for the constant-pH MD simulation including the αX I-domain from 4NEH (open Mg^{2+}-bound), 5ES4 (closed Mg^{2+}-bound), and 1N3Y (closed Mg^{2+}-free). The systems were prepared with CHARMM-GUI's Glycan Reader and Modeller tool with all crystal waters surrounding the αX I-domain included for system preparation using the CHARMM36m (charmm36-mar2019.ff) forcefield (Jo et al., 2008; Park et al., 2019). The protonation states specified for acidic and basic residues were confirmed using PROPKA3.1 with calculated values at pH 7.0 (Olsson et al., 2011). The protonation states of all HIS residues were confirmed by visually analyzing their local environments. A rectangular box with an edge length of 16 Å was used to solvate the αX I-domain using the TIP3P water model with a 0.15 mM NaCl ion concentration. The overall charge of the protein was neutralized by providing a slight excess of Na^+ or Cl^- ions, which enables the use of Particle-Mesh Ewald (PME) electrostatics. Configuration, parameter, and topology files specific to NAMD were prepared using CHARMM-GUI and subsequently used by NAMD (version 2.14) (Phillips et al., 2020) to perform conjugate gradient minimization for 10,000 steps (minLineGoal = $1.0e^{-4}$ kcal/mol). Backbone and sidechain carbon atom-constrained Langevin dynamics was utilized for equilibration as well as constant-pH MD production runs with the temperature set at 310 K and Langevin dampening coefficient set to 1.0 ps^{-1}. All three systems were simulated at 14 different pH values ranging from 0.4 to 8.4 with a separation of 0.4 units. The termini of the αX I-domain were fixed in their zwitterionic states with periodic boundary conditions (PBC) enabled, using particle mesh Ewald (PME) electrostatics with grid spacing set to 1.0 Å in all simulations. The multiple time stepping (MTS) integrator Verlet-I/r-RESPA was used with a time step of 2 fs, with length of bonds to hydrogen atoms constrained to their equilibrium length using the ShakeH algorithm and a cut-off distance of 12.0 Å with the force-switch (both switching and vdwForceSwitching enabled) distance set as 10.0 Å to smoothly transition Van der Waals (VdW) potential to 0. All systems at the different pH values were simulated for a total of 31 ns in the isothermal-isochoric (NVT) ensemble with the 1 ns discarded as equilibration. The protonation attempts were made every 10 ps over 30 ns with switch times specified as 20 ps (i.e., 3000 neMD/MC cycles). PROPKA-calculated pK_a values were assigned as the inherent pK_a values and remained constant for the duration of the entire simulation. The cphanalyze Tcl script of the pynamd package, available through NAMD, was used to analyze the cphlog files generated by the software for neMD/MC simulations. pK_a values correspond to the 50% protonation fraction calculated. The titration curves were plotted in GraphPad Prism version 9.

Born equation used to calculate local dielectric constants is

$$1.359\Delta pK_{ii} = \frac{322}{2 \cdot r_{cavity}} \cdot \left(\frac{1}{\varepsilon_{ff}} - \frac{1}{\varepsilon_{H_2O} \cdot e^{K \cdot r_{cavity}}} \right)$$

where κ is the Debye–Hückel parameter, r_{cavity} is the cavity radius of the charged atom, ε_{H_2O} = 78.3, and ΔpK_{ii} is the difference in the pK_a values.

Circular dichroism (CD)—Perturbation observed in our RCC network analysis (Figure 4E) encompasses residues that are exclusively located in helices and loops and undergo local folding/unfolding transitions in X-ray structures. Thus, we tested whether Mg^{2+}-binding in-solution alters the secondary structure content of the αX I-domain using circular dichroism (CD). Briefly, the ensemble-averaged secondary structure changes of αX I-domains showed a Mg^{2+}-induced loss of overall helicity (Figures S4A–S4C). Given that the CD contribution and significant geometric variability of secondary structures from non-peptidic chromophores were absent in the acquired data (Figure S4D, related to Figure 5D), the observed reduction in helical content is clearly driven by Mg^{2+}-binding.

Olis DSM 1000 CD was calibrated with 2.4 mM ammonium (+)-10-ncamphorsulfonate. CD experiments were conducted at 10 μM concentration of the αX I-domain in a 1 mm cuvette using 2400 lines/mm grating and slit of 1.24 mm width, followed by normalization against the buffer spectra. Each spectrum was an average of at least three scans. The mean residue molar ellipticity was calculated from the observed ellipticities according to the following equation:

$$\theta = \frac{\theta_0 \underline{w}_{res}}{10/c} \# \quad \text{(Equation 2)}$$

where θ is the mean residue molar ellipticity in deg·cm^2·dmol^{-1}, θ_0 is the observed ellipticity in millidegrees, $\underline{w}_{res}$ is the mean residue weight (MRW) of the αX I-domains (molecular mass/[Number of amino acids − 1]), l is the path length in centimeters, and c is the αX I-domain concentration in g/L. The secondary structure content was calculated using the CD Pro suite with the reference set of SP37A. Three different algorithms (SELCON, CONTIN-LL, and CDSSTR) were implemented for the analysis (Sreerama and Woody, 2000, 2004).

Small Angle X-ray scattering—A large stock volume (~5 L) of the buffer (20 mM HEPES, 150 mM NaCl, pH 7.5) in metal-free water was prepared, and the αX I-domain was purified with identical buffer in the last step of size exclusion chromatography (SEC) purification. The SEC eluted fractions of the αX I-domain were concentrated and spun down to remove precipitations such that a final αX I-domain stock concentration of 2.5 mg/mL. 500 μL protein was then dialyzed against one of 11 buffers in 250 mL containing 0 μM, 20 μM, 100 μM, 250 μM, 500 μM, 3 mM, 10 mM, 20 mM, 60 mM, 100 mM, and 250 mM Mg^{2+} in a dialysis bag of 10 kDa molecular mass cut-off (MilliporeSigma). The dialysis was carried out overnight with gentle stirring at 4°C. The resulting αX I-domain sample was spun to remove any precipitation, aliquoted at 70 μL each for three replicates, vitrified in liquid nitrogen, and shipped on dry-ice to NSLS-II. In control experiments, freeze-thawed and unfrozen αX I-domain samples at each $MgCl_2$ concentration displayed identical elution profiles, showing that no precipitation or aggregation occurred during the freeze-thaw process. For the SEC-SAXS experiment, 100 μL of 10 mg/mL αX I-domain was injected into the Superdex S200 column for each experimental run using a Shimadzu HPLC system at a flow rate of 0.5mL/min. A total of 360 frames were collected with an exposure of 2seconds. The running buffer was the SEC buffer (20 mM HEPES, 150 mM NaCl, pH 7.5) containing 20 μM, 100 μM, 250 μM, 500 μM, and 3 mM $MgCl_2$

concentrations. Similarly, aside from R_g and D_{max} enlargement in dynamic SEC-SAXS measurements, the hydrodynamic radius simultaneously showed a biphasic transition, as reflected by bimodal change in the retention times of different Mg^{2+}-concentrations (Figure S4G, related to the STAR methods section, Small Angle X-ray Scattering). The SAXS experiments were collected using National Synchrotron Light Source-II (NSLS-II) Beamline 16-ID (LiX) at Brookhaven National Laboratory[108]. Guinier plots and P(r) function was calculated using GNOM from ATSAS and determination of the regularization parameter in indirect-transform methods using perceptual criteria (Franke et al., 2017). Each Mg^{2+}/αX I-domain dataset displayed characteristics of a compact globular scattering biomolecule in solution.

Nuclear magnetic resonance—^{15}N-^{13}C or ^{15}N-^{13}C-^{2}D labelled αX I-domains were expressed as described previously (Sen and Legge, 2007). After Ni-NTA and size exclusion chromatography, the αX I-domain was concentrated to 10 mg/mL and buffer exchanged to 20 mM MES pH 7.0, 10% D_2O with or without Mg^{2+}. NMR spectra of an isotopically labelled αX I-domain were acquired on an 800 MHz Bruker (operating at a ^{1}H frequency of 800.013 MHz equipped with a TCI cryoprobe) and a 600 MHz Bruker Spectrometers (operating at a ^{1}H frequency of 599.878 Mhz) equipped with a three-channel inverse TXI probe. Triple-resonance experiments, HNCA, HN(CO)CA, HNCACB, CBCA(CO)NH, HNCO, and HN(CA)CO experiments were used to obtain the chemical shift assignments of the αX I-domain residues. All spectra were processed using NMRPipe (Delaglio et al., 1995) and subsequently analysed with Sparky.

Surface plasmon resonance (SPR)—All SPR data collection was performed on a Biacore X100 instrument (GE Healthcare) at 25°C using running buffer containing 20 mM HEPES, 150 mM NaCl, pH 7.5. To ensure that the running buffer is metal-free, MilliQ-water was treated with Chelex-100, chelating resin binding polyvalent metal ions. 50 μg/mL fibrinogen in 10 mM sodium acetate pH 4.5 were immobilized via amine coupling onto CM1 chip with 5491.2 RU at a flow rate of 5 μL/min. As reference, an activated flow cell was blocked with ethylenediamine. Interaction of the 10 μM αX I-domains with the ligand-coated- or control surface was tested at different Mg^{2+} concentrations in running buffer containing 20 mM HEPES, 150 mM NaCl, pH 7.5 prepared in cation-free water. Affinity measurements were performed in the running buffer containing respective Mg^{2+} concentrations; The αX I-domain was diluted in HBS buffer containing 100 μM, 500 μM, 5 mM, 10 mM, and 50 mM Mg^{2+} and injected in a random series of 11 concentrations (39 nM-40 μM) at a flow rate of 10 μL/min. The elapsed time for binding was 450 seconds, 400 seconds for dissociation, and 230 seconds for regeneration. Regeneration was achieved in buffer containing 100 mM HEPES, 0.5 M NaCl, and 150 mM EDTA pH 7.0. In data analysis, first, the sensorgrams were preprocessed for baseline adjustment, and reference cell signal subtraction using Bia-evaluation followed by correction of the injection time using the software Scrubber. Here, it is important to note that previously, typical SPR data for the αM I-domain–the sister-homolog of the αX I-domain–displayed nonconformity with simple binding models (Bajic et al., 2013). Therefore, binding-traces were loaded into the EVILFIT (Gorshkova et al., 2008) and were globally fit for all concentrations using

Tikhonov regularization. The boundaries for the distributions were uniformly set to K_d values in the interval from 10^{-9} to 10^{0} s^{-1} and K_d values in the interval from 10^{-9} to 10^{0} M.

E-IgM-iC3b rosetting assay—Sheep erythrocytes (Colorado Serum Co. 31112) were sensitized with IgM(E-IgM) and with C5-deficient human complement (E-IgM-iC3b) as previously established (Bilsland et al., 1994). Briefly, sheep erythrocytes were washed once with PBS (pH7.4), then incubated with anti-Forssman IgM monoclonal antibody (M1/87) (RRID: AB_2109207) for one hour at room temperature. Then, the E-IgM complex was incubated with C5- deficient human serum at 37°C for 1 hr. E-IgM-iC3b and E-IgM, being utilized as controls, were assessed for binding to αXβ2 HEK293T transfectants. After 48 hours of transfection, cells in a 24 well plate were washed once with Hepes-Buffered Saline (HBS) and incubated with 1mM Mn^{2+}/0.2mM Ca^{2+} and varying Mg^{2+}/1mM Ca^{2+} for 30 mins at room temperature. To eliminate the effect of the β2 I-domain on the αXβ2-affinity, we used either inhibitory monoclonal mAb, 10 μg/ml TS1/18 (RRID: AB_628939), or 1 μM small-molecule inhibitor XVA143. E-IgM-iC3b (250uL) was then added and the plate was incubated for 1.5 hrs at 37°C. Unbound erythrocytes were removed by gentle washing (3x) with HBS supplemented with either (1mM Mn^{2+}/0.2mM Ca^{2+}) or (1mM Mg^{2+}/1mM Ca^{2+}). Rosettes (>10 erythrocytes/HEK293T cell) were scored by microscopy.

QUANTIFICATION AND STATISTICAL ANALYSIS

All binding data are presented as mean ± standard error of the mean. Statistical analyses were performed using t-test for the comparison of two groups. Data analyses were performed using GraphPad Prism 7 (GraphPad Software). $p < 0.05$ was considered significant. p values were presented as $p > 0.05$ (ns, not significant).

Supplementary Material

Refer to Web version on PubMed Central for supplementary material.

ACKNOWLEDGMENTS

This work was supported by NIH grant NIAID R03 AI139651 and the National University Research Fund (to M.S.). We thank Zhang Weihua, William Widger, and Emiliano Pinelo for their critical insights, and Muneera Beach and Verna Frasca for DSC data acquisition and data analysis. This work was completed in part with resources provided by the Research Computing Data Core at the University of Houston. We also thank the NSLS-II beamline 16-ID (LiX) staff at the Brookhaven National Lab. The LiX beamline is part of the Center for BioMolecular Structure (CBMS) and is supported primarily by the National Institutes of Health (NIH), National Institute of General Medical Sciences (NIGMS) through a P30 grant (P30GM133893) and by the Department of Energy Office of Biological and Environmental Research (KP1605010). LiX also received additional support from NIH grant S10 OD012331. As part of NSLS-II, a national user facility at Brookhaven National Laboratory, work performed at the CBMS is supported in part by the US Department of Energy, Office of Science, Office of Basic Energy Sciences Program under contract number DE-SC0012704.

REFERENCES

Adebamowo SN, Spiegelman D, Willett WC, and Rexrode KM (2015). Association between intakes of magnesium, potassium, and calcium and risk of stroke: 2 cohorts of US women and updated meta-analyses. Am. J. Clin. Nutr 101, 1269–1277. 10.3945/ajcn.114.100354. [PubMed: 25948665]

Ajroud K, Sugimori T, Goldmann WH, Fathallah DM, Xiong JP, and Arnaout MA (2004). Binding affinity of metal ions to the CD11b A-domain is regulated by integrin activation and ligands. J. Biol. Chem 279, 25483–25488. 10.1074/jbc.M402901200. [PubMed: 15070893]

Azcutia V, Routledge M, Williams MR, Newton G, Frazier WA, Manica A, Croce KJ, Parkos CA, Schmider AB, Turman MV, et al. (2013). CD47 plays a critical role in T-cell recruitment by regulation of LFA-1 and VLA-4 integrin adhesive functions. Mol. Biol. Cell 24, 3358–3368. 10.1091/mbc.E13-01-0063. [PubMed: 24006483]

Bajic G, Yatime L, Sim RB, Vorup-Jensen T, and Andersen GR (2013). Structural insight on the recognition of surface-bound opsonins by the integrin I domain of complement receptor 3. Proc. Natl. Acad. Sci. USA 110, 16426–16431. 10.1073/pnas.1311261110. [PubMed: 24065820]

Baldwin ET, Sarver RW, Bryant GL Jr., Curry KA, Fairbanks MB, Finzel BC, Garlick RL, Heinrikson RL, Horton NC, Kelley LL, et al. (1998). Cation binding to the integrin CD11b I domain and activation model assessment. Structure 6, 923–935. 10.1016/s0969-2126(98)00093-8. [PubMed: 9687375]

Bilsland CA, Diamond MS, and Springer TA (1994). The leukocyte integrin p150, 95 (CD11c/CD18) as a receptor for iC3b. Activation by a heterologous beta subunit and localization of a ligand recognition site to the I domain. J. Immunol 152, 4582–4589. [PubMed: 7512600]

Bondu V, Wu C, Cao W, Simons PC, Gillette J, Zhu J, Erb L, Zhang XF, and Buranda T (2017). Low-affinity binding in cis to P2Y2R mediates force-dependent integrin activation during hantavirus infection. Mol. Biol. Cell 28, 2887–2903. 10.1091/mbc.E17-01-0082. [PubMed: 28835374]

Bryngelson JD, and Wolynes PG (1987). Spin glasses and the statistical mechanics of protein folding. Proc. Natl. Acad. Sci. USA 84, 7524–7528. 10.1073/pnas.84.21.7524. [PubMed: 3478708]

Bumiller-Bini V, Cipolla GA, de Almeida RC, Petzl-Erler ML, Augusto DG, and Boldt ABW (2018). Sparking fire under the skin? Answers from the association of complement genes with Pemphigus foliaceus. Front. Immunol 9, 695. 10.3389/fimmu.2018.00695. [PubMed: 29686679]

Calderwood DA, Tuckwell DS, Eble J, Kühn K, and Humphries MJ (1997). The integrin alpha1 A-domain is a ligand binding site for collagens and laminin. J. Biol. Chem 272, 12311–12317. 10.1074/jbc.272.19.12311. [PubMed: 9139675]

Castiglioni S, Cazzaniga A, Albisetti W, and Maier JAM (2013). Magnesium and osteoporosis: current state of knowledge and future research directions. Nutrients 5, 3022–3033. 10.3390/nu5083022. [PubMed: 23912329]

Caswell PT, Vadrevu S, and Norman JC (2009). Integrins: masters and slaves of endocytic transport. Nat. Rev. Mol. Cell Biol 10, 843–853. 10.1038/nrm2799. [PubMed: 19904298]

Chen Y, and Roux B (2015). Constant-pH hybrid nonequilibrium molecular dynamics-Monte Carlo simulation method. J. Chem. Theor. Comput 11, 3919–3931. 10.1021/acs.jctc.5b00261.

Delaglio F, Grzesiek S, Vuister GW, Zhu G, Pfeifer J, and Bax A (1995). NMRPipe: a multidimensional spectral processing system based on UNIX pipes. J. Biomol. NMR 6, 277–293. [PubMed: 8520220]

Di Russo NV, Estrin DA, Martí MA, and Roitberg AE (2012). pH-Dependent conformational changes in proteins and their effect on experimental pK(a)s: the case of Nitrophorin 4. PLoS Comput. Biol 8, e1002761. 10.1371/journal.pcbi.1002761. [PubMed: 23133364]

Dong J, Dong L, Méndez E, and Tao Y (2011). Crystal structure of the human astrovirus capsid spike. Proc. Natl. Acad. Sci. USA 108, 12681–12686. 10.1073/pnas.1104834108. [PubMed: 21768348]

Dong X, Hudson NE, Lu C, and Springer TA (2014). Structural determinants of integrin beta-subunit specificity for latent TGF-beta. Nat. Struct. Mol. Biol 21, 1091–1096. 10.1038/nsmb.2905. [PubMed: 25383667]

Dong X, Mi LZ, Zhu J, Wang W, Hu P, Luo BH, and Springer TA (2012). alpha(V)beta(3) integrin crystal structures and their functional implications. Biochemistry 51, 8814–8828. 10.1021/bi300734n. [PubMed: 23106217]

Dransfield I, Cabañas C, Craig A, and Hogg N (1992). Divalent cation regulation of the function of the leukocyte integrin LFA-1. J. Cell Biol 116, 219–226. 10.1083/jcb.116.1.219. [PubMed: 1346139]

Dutta AK, Rösgen J, and Rajarathnam K (2015). Using isothermal titration calorimetry to determine thermodynamic parameters of protein-glycosaminoglycan interactions. Methods Mol. Biol 1229, 315–324. 10.1007/978-1-4939-1714-3_25. [PubMed: 25325962]

Duvvuri H, Wheeler LC, and Harms MJ (2018). Pytc: open-source Python software for global analyses of isothermal titration calorimetry data. Biochemistry 57, 2578–2583. 10.1021/acs.biochem.7b01264. [PubMed: 29620867]

Fan Z, Kiosses WB, Sun H, Orecchioni M, Ghosheh Y, Zajonc DM, Arnaout MA, Gutierrez E, Groisman A, Ginsberg MH, and Ley K (2019). High-affinity bent beta2-integrin molecules in arresting neutrophils face each other through binding to ICAMs in cis. Cell Rep. 26, 119–130.e5. 10.1016/j.celrep.2018.12.038. [PubMed: 30605669]

Fan Z, McArdle S, Marki A, Mikulski Z, Gutierrez E, Engelhardt B, Deutsch U, Ginsberg M, Groisman A, and Ley K (2016). Neutrophil recruitment limited by high-affinity bent beta2 integrin binding ligand in cis. Nat. Commun 7, 12658. 10.1038/ncomms12658. [PubMed: 27578049]

Fiore VF, Strane PW, Bryksin AV, White ES, Hagood JS, and Barker TH (2015). Conformational coupling of integrin and Thy-1 regulates Fyn priming and fibroblast mechanotransduction. J. Cell Biol 211, 173–190. 10.1083/jcb.201505007. [PubMed: 26459603]

Fiore VF, Wong SS, Tran C, Tan C, Xu W, Sulchek T, White ES, Hagood JS, and Barker TH (2018). alphavbeta3 Integrin drives fibroblast contraction and strain stiffening of soft provisional matrix during progressive fibrosis. JCI Insight 3, 97597. 10.1172/jci.insight.97597. [PubMed: 30333317]

Franke D, Petoukhov MV, Konarev PV, Panjkovich A, Tuukkanen A, Mertens HDT, Kikhney AG, Hajizadeh NR, Franklin JM, Jeffries CM, and Svergun DI (2017). Atsas 2.8: a comprehensive data analysis suite for small-angle scattering from macromolecular solutions. J. Appl. Crystallogr 50, 1212–1225. 10.1107/S1600576717007786. [PubMed: 28808438]

Fu X, Xu Y, Wu C, Moy VT, and Zhang XF (2015). Anchorage-dependent binding of integrin I-domain to adhesion ligands. J. Mol. Recognit 28, 385–392. 10.1002/jmr.2453. [PubMed: 25707989]

Gang J, Choi J, Lee JH, and Nham SU (2007). Identification of critical residues for plasminogen binding by the alphaX I-domain of the beta2 integrin, alphaXbeta2. Mol. Cells 24, 240–246. [PubMed: 17978577]

García-Moreno BE, Dwyer JJ, Gittis AG, Lattman EE, Spencer DS, and Stites WE (1997). Experimental measurement of the effective dielectric in the hydrophobic core of a protein. Biophys. Chem 64, 211–224. 10.1016/S0301-4622(96)02238-7. [PubMed: 9127946]

Gorshkova II, Svitel J, Razjouyan F, and Schuck P (2008). Bayesian analysis of heterogeneity in the distribution of binding properties of immobilized surface sites. Langmuir 24, 11577–11586. 10.1021/la801186w. [PubMed: 18816013]

Grant BJ, Skjaerven L, and Yao XQ (2021). The Bio3D packages for structural bioinformatics. Protein Sci. 30, 20–30. 10.1002/pro.3923. [PubMed: 32734663]

Grimsley GR, Scholtz JM, and Pace CN (2009). A summary of the measured pK values of the ionizable groups in folded proteins. Protein Sci. 18, 247–251. 10.1002/pro.19. [PubMed: 19177368]

Hogg N, Takacs L, Palmer DG, Selvendran Y, and Allen C (1986). The p150, 95 molecule is a marker of human mononuclear phagocytes: comparison with expression of class II molecules. Eur. J. Immunol 16, 240–248. 10.1002/eji.1830160306. [PubMed: 3456894]

Hom G, Graham RR, Modrek B, Taylor KE, Ortmann W, Garnier S, Lee AT, Chung SA, Ferreira RC, Pant PVK, et al. (2008). Association of systemic lupus erythematosus with C8orf13-BLK and ITGAM-ITGAX. N. Engl. J. Med 358, 900–909. 10.1056/NEJMoa0707865. [PubMed: 18204098]

Hynes RO (2002). Integrins: bidirectional, allosteric signaling machines. Cell 110, 673–687. [PubMed: 12297042]

Jahnen-Dechent W, and Ketteler M (2012). Magnesium basics. Clin. Kidney J 5, i3–i14. 10.1093/ndtplus/sfr163. [PubMed: 26069819]

Jensen RK, Pedersen H, Lorentzen J, Laursen NS, Vorup-Jensen T, and Andersen GR (2021). Structure of the integrin receptor αMβ2 headpiece in complex with a function-modulating nanobody. Preprint at bioRxiv. 10.1101/2021.07.07.451531.

Jin M, Song G, Carman CV, Kim YS, Astrof NS, Shimaoka M, Wittrup DK, and Springer TA (2006). Directed evolution to probe protein allostery and integrin I domains of 200, 000-fold higher affinity. Proc. Natl. Acad. Sci. USA 103, 5758–5763. 10.1073/pnas.0601164103. [PubMed: 16595626]

Jo S, Kim T, Iyer VG, and Im W (2008). CHARMM-GUI: a web-based graphical user interface for CHARMM. J. Comput. Chem 29, 1859–1865. 10.1002/jcc.20945. [PubMed: 18351591]

Kanellopoulou C, George AB, Masutani E, Cannons JL, Ravell JC, Yamamoto TN, Smelkinson MG, Jiang PD, Matsuda-Lennikov M, Reilley J, et al. (2019). Mg(2+) regulation of kinase signaling and immune function. J. Exp. Med 216, 1828–1842. 10.1084/jem.20181970. [PubMed: 31196981]

Karp DA, Gittis AG, Stahley MR, Fitch CA, Stites WE, and García-Moreno E B (2007). High apparent dielectric constant inside a protein reflects structural reorganization coupled to the ionization of an internal Asp. Biophys. J 92, 2041–2053. 10.1529/biophysj.106.090266. [PubMed: 17172297]

Kharitidi D, Apaja PM, Manteghi S, Suzuki K, Malitskaya E, Roldan A, Gingras MC, Takagi J, Lukacs GL, and Pause A (2015). Interplay of endosomal pH and ligand occupancy in integrin alpha5beta1 ubiquitination, endocytic sorting, and cell migration. Cell Rep. 13, 599–609. 10.1016/j.celrep.2015.09.024. [PubMed: 26456826]

Kiryluk K, Li Y, Sanna-Cherchi S, Rohanizadegan M, Suzuki H, Eitner F, Snyder HJ, Choi M, Hou P, Scolari F, et al. (2012). Geographic differences in genetic susceptibility to IgA nephropathy: GWAS replication study and geospatial risk analysis. PLoS Genet. 8, e1002765. 10.1371/journal.pgen.1002765. [PubMed: 22737082]

Leitinger B, McDowall A, Stanley P, and Hogg N (2000). The regulation of integrin function by Ca(2+). Biochim. Biophys. Acta 1498, 91–98. 10.1016/s0167-4889(00)00086-0. [PubMed: 11108953]

Lotscher J, Martí I Líndez AA, Kirchhammer N, Cribioli E, Giordano Attianese GMP, Trefny MP, Lenz M, Rothschild SI, Strati P, Künzli M, et al. (2022). Magnesium sensing via LFA-1 regulates CD8(+) T cell effector function. Cell 185, 585–602.e29. 10.1016/j.cell.2021.12.039. [PubMed: 35051368]

Lu C, Shimaoka M, Zang Q, Takagi J, and Springer TA (2001). Locking in alternate conformations of the integrin alphaLbeta2 I domain with disulfide bonds reveals functional relationships among integrin domains. Proc. Natl. Acad. Sci. USA 98, 2393–2398. 10.1073/pnas.041618598. [PubMed: 11226250]

Mahalingam B, Ajroud K, Alonso JL, Anand S, Adair BD, Horenstein AL, Malavasi F, Xiong JP, and Arnaout MA (2011). Stable coordination of the inhibitory Ca2+ ion at the metal ion-dependent adhesion site in integrin CD11b/CD18 by an antibody-derived ligand aspartate: implications for integrin regulation and structure-based drug design. J. Immunol 187, 6393–6401. 10.4049/jimmunol.1102394. [PubMed: 22095715]

Monera OD, Sereda TJ, Zhou NE, Kay CM, and Hodges RS (1995). Relationship of sidechain hydrophobicity and alpha-helical propensity on the stability of the single-stranded amphipathic alpha-helix. J. Pept. Sci 1, 319–329. 10.1002/psc.310010507. [PubMed: 9223011]

Montero M, Brini M, Marsault R, Alvarez J, Sitia R, Pozzan T, and Rizzuto R (1995). Monitoring dynamic changes in free Ca2+ concentration in the endoplasmic reticulum of intact cells. EMBO J. 14, 5467–5475. [PubMed: 8521803]

Nayal M, and Di Cera E (1994). Predicting Ca(2+)-binding sites in proteins. Proc. Natl. Acad. Sci. USA 91, 817–821. 10.1073/pnas.91.2.817. [PubMed: 8290605]

Nordenfelt P, Moore TI, Mehta SB, Kalappurakkal JM, Swaminathan V, Koga N, Lambert TJ, Baker D, Waters JC, Oldenbourg R, et al. (2017). Direction of actin flow dictates integrin LFA-1 orientation during leukocyte migration. Nat. Commun 8, 2047. 10.1038/s41467-017-01848-y. [PubMed: 29229906]

Olsson MHM, Søndergaard CR, Rostkowski M, and Jensen JH (2011). PROPKA3: consistent treatment of internal and surface residues in empirical pKa predictions. J. Chem. Theory Comput 7, 525–537. 10.1021/ct100578z. [PubMed: 26596171]

Park SJ, Lee J, Qi Y, Kern NR, Lee HS, Jo S, Joung I, Joo K, Lee J, and Im W (2019). CHARMM-GUI Glycan Modeler for modeling and simulation of carbohydrates and glycoconjugates. Glycobiology 29, 320–331. 10.1093/glycob/cwz003. [PubMed: 30689864]

Park SR, Park KS, Park YJ, Bang D, and Lee ES (2014). CD11a, CD11c, and CD18 gene polymorphisms and susceptibility to Behcet's disease in Koreans. Tissue Antigens 84, 398–404. 10.1111/tan.12420. [PubMed: 25155097]

Phillips JC, Hardy DJ, Maia JDC, Stone JE, Ribeiro JV, Bernardi RC, Buch R, Fiorin G, Hénin J, Jiang W, et al. (2020). Scalable molecular dynamics on CPU and GPU architectures with NAMD. J. Chem. Phys 153, 044130. 10.1063/5.0014475. [PubMed: 32752662]

Piper RC, Dikic I, and Lukacs GL (2014). Ubiquitin-dependent sorting in endocytosis. Cold Spring Harb. Perspect. Biol 6, a016808. 10.1101/cshperspect.a016808. [PubMed: 24384571]

Rabb H, Michishita M, Sharma CP, Brown D, and Arnaout MA (1993). Cytoplasmic tails of human complement receptor type 3 (CR3, CD11b/CD18) regulate ligand avidity and the internalization of occupied receptors. J. Immunol 151, 990–1002. [PubMed: 8101539]

Saggu G, Okubo K, Chen Y, Vattepu R, Tsuboi N, Rosetti F, Cullere X, Washburn N, Tahir S, Rosado AM, et al. (2018). Cis interaction between sialylated FcgammaRIIA and the alphaI-domain of Mac-1 limits antibody-mediated neutrophil recruitment. Nat. Commun 9, 5058. 10.1038/s41467-018-07506-1. [PubMed: 30498196]

San Sebastian E, Mercero JM, Stote RH, Dejaegere A, Cossío FP, and Lopez X (2006). On the affinity regulation of the metal-ion-dependent adhesion sites in integrins. J. Am. Chem. Soc 128, 3554–3563. 10.1021/ja054142a. [PubMed: 16536528]

Saris NE, Mervaala E, Karppanen H, Khawaja JA, and Lewenstam A (2000). Magnesium. An update on physiological, clinical and analytical aspects. Clin. Chim. Acta 294, 1–26. 10.1016/s0009-8981(99)00258-2. [PubMed: 10727669]

Schymkowitz JWH, Rousseau F, Martins IC, Ferkinghoff-Borg J, Stricher F, and Serrano L (2005). Prediction of water and metal binding sites and their affinities by using the Fold-X force field. Proc. Natl. Acad. Sci. USA 102, 10147–10152. 10.1073/pnas.0501980102. [PubMed: 16006526]

Sen M, Koksal AC, Yuki K, Wang J, and Springer TA (2018). Ligand- and cation-induced structural alterations of the leukocyte integrin LFA-1. Journal of Biological Chemistry 293, 6565–6577. 10.1074/jbc.RA117.000710. [PubMed: 29507098]

Sen M, and Legge GB (2007). Pactolus I-domain: functional switching of the Rossmann fold. Proteins 68, 626–635. 10.1002/prot.21458. [PubMed: 17523188]

Sen M, and Springer TA (2016). Leukocyte integrin alphaLbeta2 headpiece structures: the alphaI domain, the pocket for the internal ligand, and concerted movements of its loops. Proc. Natl. Acad. Sci. USA 113, 2940–2945. 10.1073/pnas.1601379113. [PubMed: 26936951]

Sen M, Yuki K, and Springer TA (2013). An internal ligand-bound, meta-stable state of a leukocyte integrin, alphaXbeta2. J. Cell Biol 203, 629–642. 10.1083/jcb.201308083. [PubMed: 24385486]

Shamri R, Grabovsky V, Gauguet JM, Feigelson S, Manevich E, Kolanus W, Robinson MK, Staunton DE, von Andrian UH, and Alon R (2005). Lymphocyte arrest requires instantaneous induction of an extended LFA-1 conformation mediated by endothelium-bound chemokines. Nat. Immunol 6, 497–506. [PubMed: 15834409]

Shannon RD (1976). Revised effective ionic radii and systematic studies of interatomic distances in halides and chalcogenides. Acta Cryst. Sect. A 32, 751–767. 10.1107/S0567739476001551.

Sheikh S, and Nash GB (1996). Continuous activation and deactivation of integrin CD11b/CD18 during de novo expression enables rolling neutrophils to immobilize on platelets. Blood 87, 5040–5050. [PubMed: 8652817]

Shimaoka M, Xiao T, Liu JH, Yang Y, Dong Y, Jun CD, McCormack A, Zhang R, Joachimiak A, Takagi J, et al. (2003). Structures of the αL I domain and its complex with ICAM-1 reveal a shape-shifting pathway for integrin regulation. Cell 112, 99–111. [PubMed: 12526797]

Shrake A, and Ross PD (1988). Biphasic denaturation of human albumin due to ligand redistribution during unfolding. J. Biol. Chem 263, 15392–15399. [PubMed: 3170588]

Springer TA, and Dustin ML (2012). Integrin inside-out signaling and the immunological synapse. Curr. Opin. Cell Biol 24, 107–115. 10.1016/j.ceb.2011.10.004. [PubMed: 22129583]

Sreerama N, and Woody RW (2000). Estimation of protein secondary structure from circular dichroism spectra: comparison of CONTIN, SELCON, and CDSSTR methods with an expanded reference set. Anal. Biochem 287, 252–260. 10.1006/abio.2000.4880. [PubMed: 11112271]

Sreerama N, and Woody RW (2004). Computation and analysis of protein circular dichroism spectra. Methods Enzymol. 383, 318–351. 10.1016/S0076-6879(04)83013-1. [PubMed: 15063656]

Tang Z, Davidson D, Li R, Zhong MC, Qian J, Chen J, and Veillette A (2021). Inflammatory macrophages exploit unconventional pro-phagocytic integrins for phagocytosis and anti-tumor immunity. Cell Rep. 37, 110111. 10.1016/j.celrep.2021.110111. [PubMed: 34910922]

Tiwari S, Askari JA, Humphries MJ, and Bulleid NJ (2011). Divalent cations regulate the folding and activation status of integrins during their intracellular trafficking. J. Cell Sci 124, 1672–1680. 10.1242/jcs.084483. [PubMed: 21511727]

Vorup-Jensen T, and Jensen RK (2018). Structural immunology of complement receptors 3 and 4. Front. Immunol 9, 2716. 10.3389/fimmu.2018.02716. [PubMed: 30534123]

Vorup-Jensen T, Waldron TT, Astrof N, Shimaoka M, and Springer TA (2007). The connection between metal ion affinity and ligand affinity in integrin I domains. Biochim. Biophys. Acta 1774, 1148–1155. 10.1016/j.bbapap.2007.06.014. [PubMed: 17702677]

Wang Y, Xu B, Hu WW, Chen LJ, Wu CP, Lu BF, Shen YP, and Jiang JT (2015). High expression of CD11c indicates favorable prognosis in patients with gastric cancer. World J. Gastroenterol 21, 9403–9412. 10.3748/wjg.v21.i31.9403. [PubMed: 26309367]

Wang Z, Thinn AMM, and Zhu J (2017). A pivotal role for a conserved bulky residue at the alpha1-helix of the alphaI integrin domain in ligand binding. J. Biol. Chem 292, 20756–20768. 10.1074/jbc.M117.790519. [PubMed: 29079572]

Xie C, Zhu J, Chen X, Mi L, Nishida N, and Springer TA (2010). Structure of an integrin with an alphaI domain, complement receptor type 4. EMBO J. 29, 666–679. 10.1038/emboj.2009.367. [PubMed: 20033057]

Xiong JP, Li R, Essafi M, Stehle T, and Arnaout MA (2000). An isoleucine-based allosteric switch controls affinity and shape shifting in integrin CD11b A-domain. J. Biol. Chem 275, 38762–38767. 10.1074/jbc.C000563200. [PubMed: 11034990]

Xiong JP, Mahalingham B, Alonso JL, Borrelli LA, Rui X, Anand S, Hyman BT, Rysiok T, Müller-Pompalla D, Goodman SL, and Arnaout MA (2009). Crystal structure of the complete integrin alphaVbeta3 ectodomain plus an alpha/beta transmembrane fragment. J. Cell Biol 186, 589–600. 10.1083/jcb.200905085. [PubMed: 19704023]

Yang W, Carman CV, Kim M, Salas A, Shimaoka M, and Springer TA (2006). A small molecule agonist of an integrin, alphaLbeta2. J. Biol. Chem 281, 37904–37912. 10.1074/jbc.M606888200. [PubMed: 17023419]

Zhao B, Zeng L, Zhao J, Wu Q, Dong Y, Zou F, Gan L, Wei Y, and Zhang W (2020). Association of magnesium intake with type 2 diabetes and total stroke: an updated systematic review and meta-analysis. BMJ Open 10, e032240. 10.1136/bmjopen-2019-032240.

Zhao L, Hu M, Yang L, Xu H, Song W, Qian Y, and Zhao M (2019). Quantitative association between serum/dietary magnesium and cardiovascular disease/coronary heart disease risk: a dose-response meta-analysis of prospective cohort studies. J. Cardiovasc. Pharmacol 74, 516–527. 10.1097/FJC.0000000000000739. [PubMed: 31815866]

Highlights

- Divalent cation concentration is sensed by the αX I-domain-αXβ2 ligand-binding domain
- Ranges of Mg^{2+}concentrations alter the αX I shape and help establish allostery
- Elevated Mg^{2+}concentration above its physiological level increases αXβ2 affinity
- Fine-tuning of the αXβ2-Mg^{2+} interaction likely has translational roles

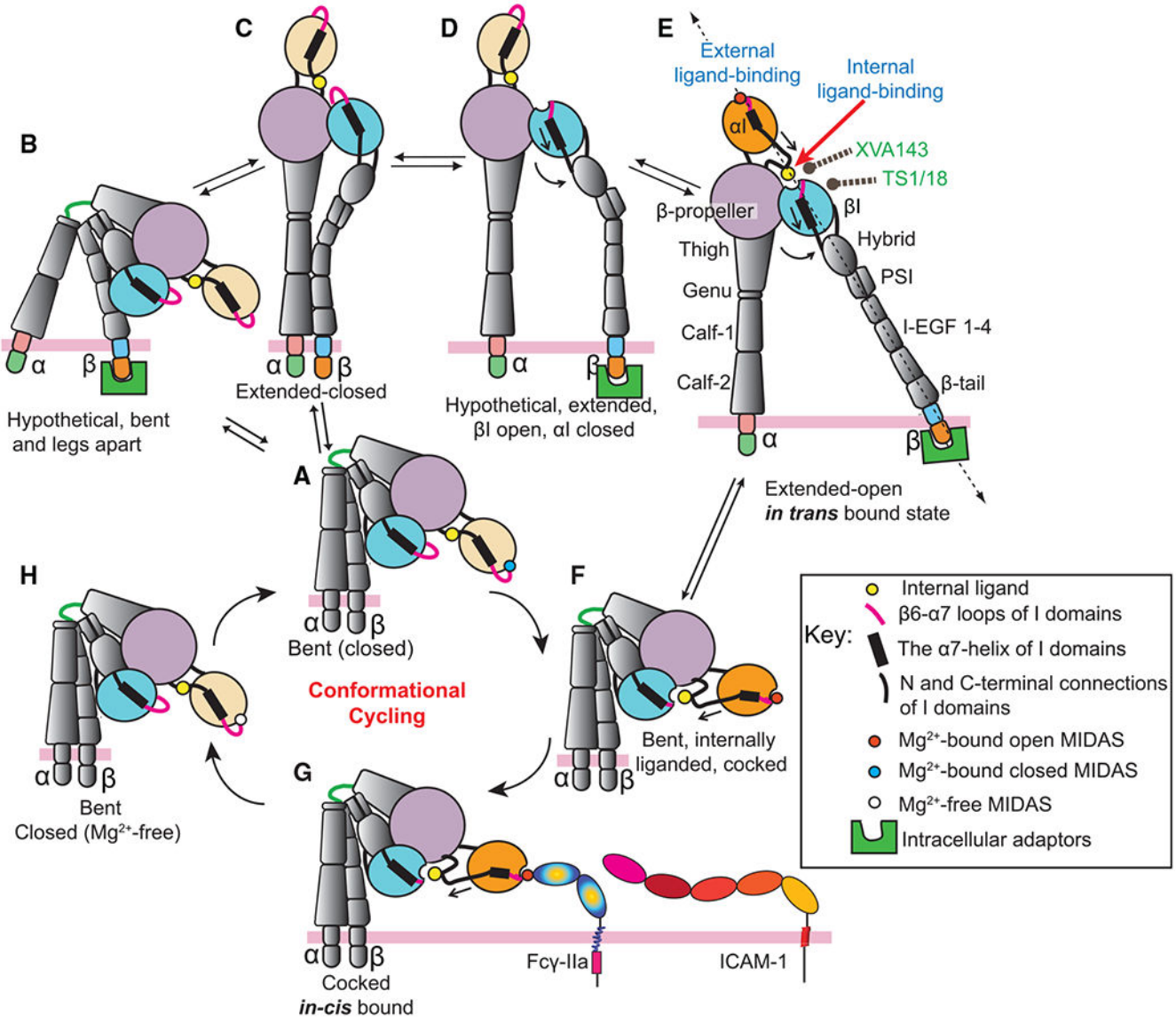

Figure 1. Schematic of the αI integrin activation mechanisms via 2 possible unique routes

Activation begins from (A) the bent/closed state and ends in (E) the extended open state. These conformational states have been observed in crystal structures, SAXS, electron microscopy, cell-based studies, or are otherwise noted as hypothetical. Route I: The bent/closed state (A) could have leg separated via the cytoplasmic adaptor binding (B) or ectodomain extension (C). The "bent and legs apart" state (B) is unlikely to exist or must be a very short-lived state. Headpiece opening and leg separation (D) would prepare the in *trans* external-ligand binding (E). Route II: In the second activation mechanism, the conformational cycling occurs starting in the (A) bent closed state and then progressing to the (F) cocked (Sen et al., 2013), (G) cocked-in *cis* bound (Saggu et al., 2018), and (H) the bent/closed-Mg^{2+}-free states sequentially. Locations of XVA143 and TS1/18 mAb bindings are labeled, and external ligands, in *trans* or ICAM-1 and Fcγ-IIa in *cis* interactions, are noted. The Mg^{2+}-free or Mg^{2+}-bound MIDAS in the closed and open αI domain, when

needed, were noted as white, blue, or red spheres, respectively. The β2-tail of the states that are available to intracellular interactions (B, D, and E) are shown to couple cytoplasmic adaptors.

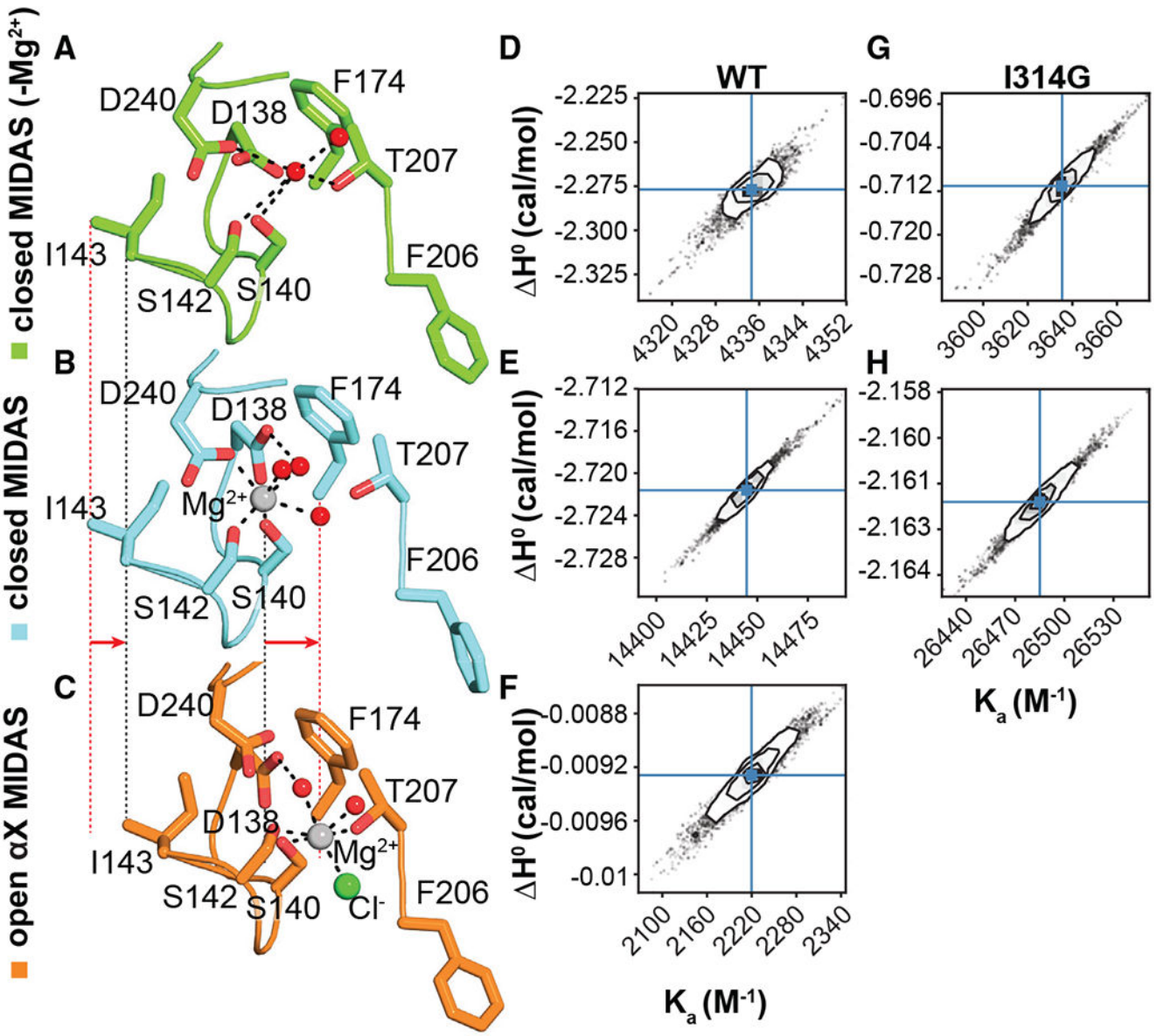

Figure 2. Dication interactions of the αX I-domain

The MIDAS assembly in the (A) Mg^{2+}-free closed (PDB: 1N3Y), (B) Mg^{2+}-bound closed (PDB: 5ES4), and (C) Mg^{2+}-bound open (PDB: 4NEH) states. Mg^{2+}, water, and CI^{-} are shown as silver, red, and green spheres, respectively. The dashed line shows the lateral movements of Mg^{2+} and I143. Interactions of (D and G) Mg^{2+}, (E and H) Mn^{2+}, and (F) Ca^{2+} with the WT αX I-domain and the I314G were probed using corner plots, showing correlations between the posterior distribution for 2 energetic parameters of the binding constant(K_a) and enthalpy ($\Delta H^0_{binding}$).

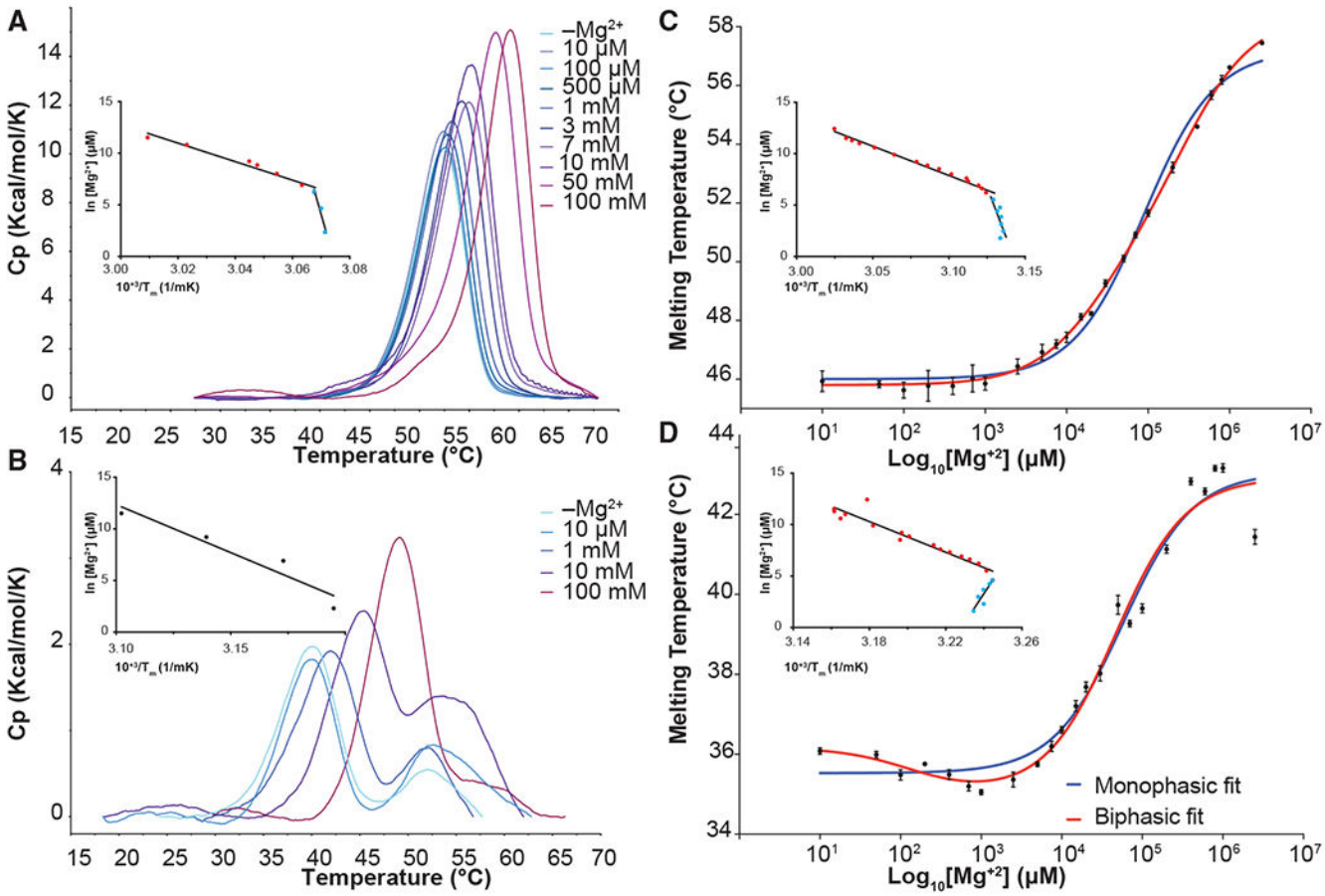

Figure 3. Effect of Mg^{2+} on the thermal stability of the αX I-domain

(A and B) DSC thermograms for the (A) WT αX I-domain and (B) I314G in increasing concentration of Mg^{2+}.

(C and D) T_m change in response to Mg^{2+}concentration from DSF denaturation for the (C) WT αX I-domain and (D) I314G were plotted and fitted to monophasic (blue) or biphasic transition (red). Plots of Van 't Hoff linear dependence between $1/T_m$ and $In[Mg^{2+}]$ are shown as the inset for the WT αX I-domain DSC and DSF dataset and the I314G construct DSF dataset.

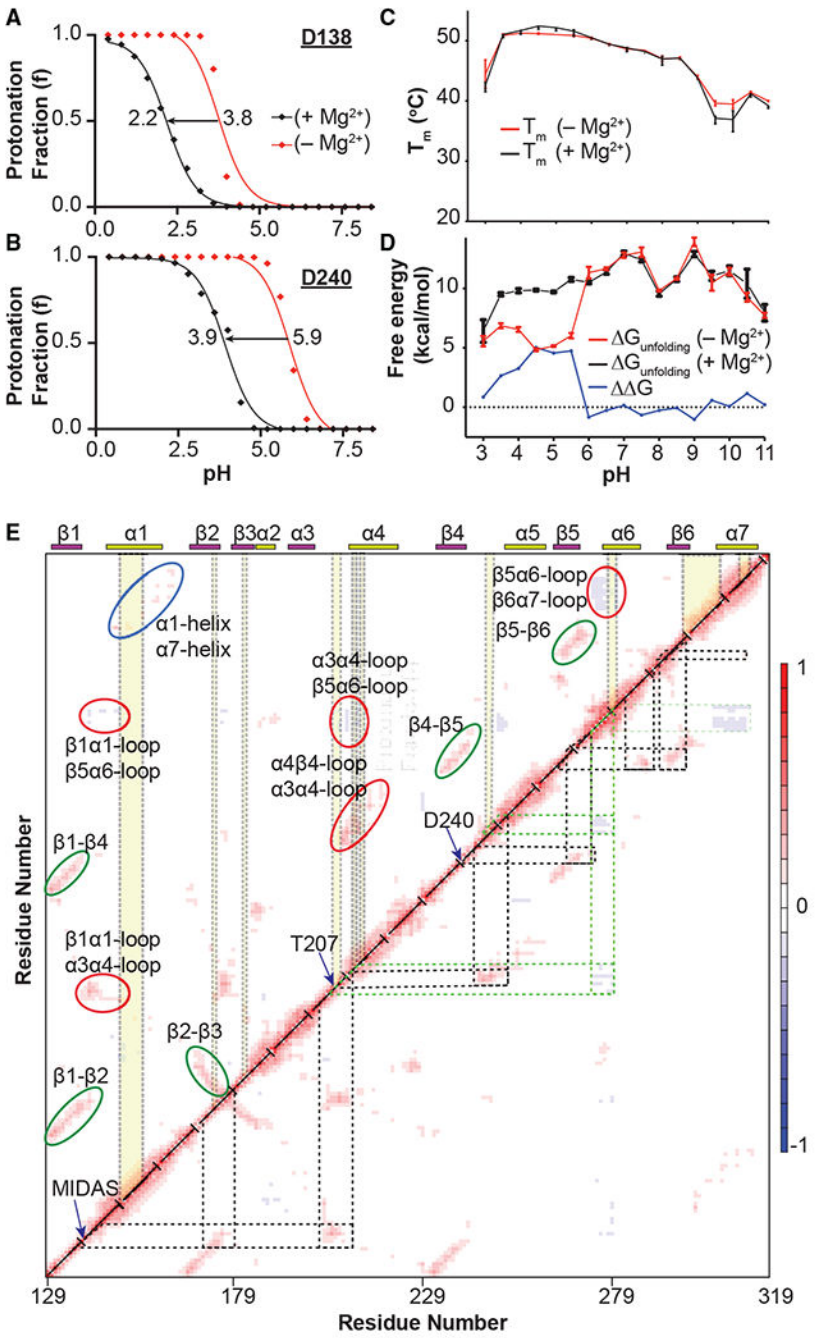

Figure 4. Probing the ionization states of the conserved MIDAS Asps and correlated motions of the αX I-domain fold

(A and B) Shifts in pK_a of (A) D138 and (B) D240 were calculated using nonequilibrium molecular dynamics and Monte Carlo simulations for the WT αX I-domain.

(C and D) Linkage analysis of pH dependence in the range of 3–11, probed by (C) the T_m change and (D) the thermodynamic stability ($\Delta G_{unfolding}$) of the WT αX I-domain in Mg^{2+}-free and 1 mM Mg^{2+}. Unfolding free energy differences shown ($\Delta\Delta G_{unfolding}$, blue line) is significant at the pH range of 3–6, and plateaus to zero at the pH values higher than 6.

(E) Residue cross-correlations (RCC) calculated from the full set of normal modes of the Mg^{2+}-bound αX I-domain Mg^{2+}. Map is color-coded, ranging from dark blue for high anticorrelations to dark red for high correlations. Routes that provide the 2 long-range coupling from MIDAS to the β6-α7 loop are drawn as black and green dashed lines, and residues that show NMR splitting are highlighted as the vertical yellow-shaded areas.

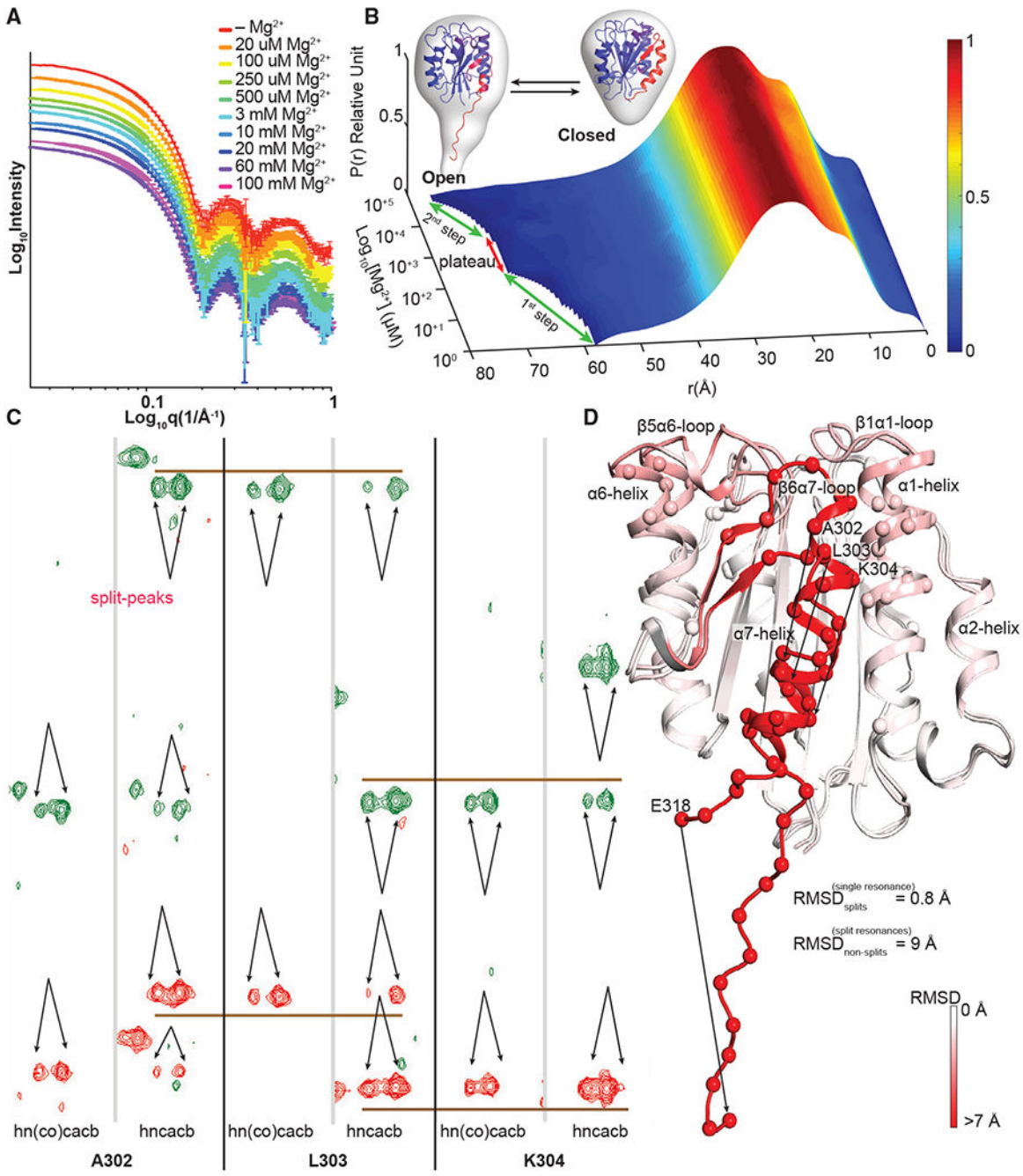

Figure 5. Effect of Mg^{2+} on the αX I-domain structure

(A and B) (A) SWAXS intensity $I(q)$ data and (B) the interpolated 3D pairwise distribution curves (P(r)) derived from the SWAXS intensity in increasing concentration of Mg^{2+}. (C) Representative strip plots from the 3D-HNCACB and HN(CO)CACB spectra, illustrating the split peaks and connectivities of $^{13}C\alpha/^{13}C\beta$ chemical shifts. The pair of HNCACB and HN(CO)CACB NMR strips for 3 exemplary residues, A302, L303, and K304, are separated by a gray line, and each residue pair is separated by a black line. The

brown lines that cross one pair to the next NMR strip indicate and validate chemical shift assignment for the Cα (red) and Cβ (green) resonances.
(D) All of the residues having split peaks are mapped to 2 closed and open states, and the Cα atoms of those residues are shown as spheres.

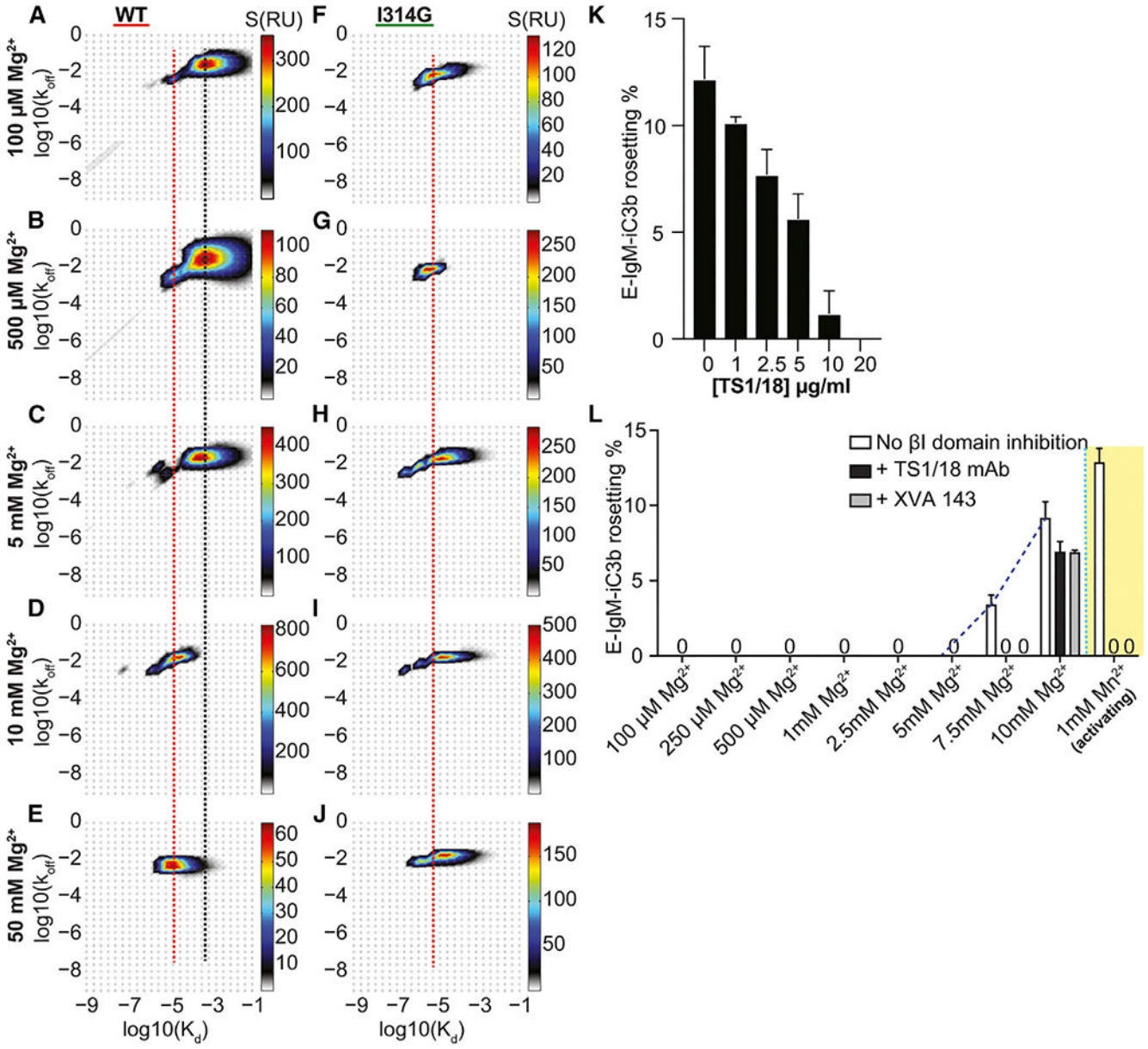

Figure 6. Effect of Mg^{2+} on αXβ2 affinity

(A–J) Distribution of the binding kinetics of fibrinogen with (A–E) the WT αX I-domain and (F–J) I314G construct in varying Mg^{2+} concentrations shown as a 2D grid (K_d and K_{off}). The black and red lines represent and are centered on the low- and high-affinity K_d values on the 2D grid.

(K and L) Inhibitory effect of TS1/18 mAb concentration on the iC3b rosetting experiment (K). Effect of the increasing concentration of Mg^{2+} ion on the cell surface expressed (L) human αXβ2 rosetting with the opsonized sheep erythrocytes. The yellow-shaded area shows the Mn^{2+}-induced αXβ2 affinity increase.

KEY RESOURCES TABLE

REAGENT or RESOURCE	SOURCE	IDENTIFIER
Bacterial and virus strains		
E. coli Rosetta BL21	EMDmillipore	Cat# 70954-3
Biological samples		
SHEEP Red Blood Cells IN ALSEVERS 60ML	FISHER SCIENTIFIC	Cat# NC9782304
Chemicals, peptides, and recombinant proteins		
SYPRO Orange Protein Gel Stain	Sigma Aldrich	SKU# S5692
(1*R*)-(−)-10-Camphorsulfonic acid ammonium salt	Sigma Aldrich	Cat# 188360
Critical commercial assays		
BCA Protein Assay Kit	Thermofisher Scientific	Cat# 23225
Experimental models: Cell lines		
HEK293T	ATCC	Cat# CRL-3216
Software and algorithms		
GraphPad Prism version 7	GraphPad Software	https://www.graphpad.com/
ATSAS 2.8	SAXS software	https://www.embl-hamburg.de/biosaxs/download.html
NMRPipe	NMR data processing	https://www.ibbr.umd.edu/nmrpipe/
Sparky	NMR data analysis	https://www.cgl.ucsf.edu/home/sparky/
ImageJ	National Institute of Health	https://imagej.nih.gov/ij/
Other		
Hard-Shell 96-Well PCR Plates	Bio-Rad	Cat# HSP9601